Australian Government
Department of Defence
Defence Science and
Technology Organisation

Experimental Study of Blast Mitigation in a Water Mist

A.D. Resnyansky and T.G. Delaney

Weapons Systems Division
Defence Science and Technology Organisation

DSTO-TR-1944

ABSTRACT

This report presents results of experiments on the mitigation of explosive blast using water mist. Water mists in the present study were produced by nozzles distributed around a test arena. Tests were conducted using different water mist sizes and nozzle arangements to evaluate blast mitigation effects for in-air bare explosive charges as well as charges submerged in water and glycerine. The effects on blast wave pressure results due to the experimental blast pressure gauge mounting and set-up, as well as due to the effects of confinement in the test area, are analysed and discussed. Blast attenuation was evaluated using the CTH hydrocode and concluded that the phase transformation and mitigant liquid breakdown mechanisms, under expansion by the blast products, must be considered in order to model blast mitigation adequately and to accurately evaluate mitigation effects at large stand-off distances.

Published by

Weapons Systems Division
DSTO Defence Science and Technology Organisation
PO Box 1500
Edinburgh South Australia 5111 Australia

Telephone: (08) 8259 5555
Fax: (08) 8259 6567

AR-013-799
November 2006

APPROVED FOR PUBLIC RELEASE

Experimental Study of Blast Mitigation in a Water Mist

Executive Summary

The increasing threat of Improvised Explosive Devices (IED) to both the military and civilians is a stimulus for researchers to seek methods that will neutralise IEDs while containing collateral damage. One of the most popular approaches to the problem of explosive blast is by mitigation using various shields including water and water mist. Generally, an increase in the ratio of the mitigant-to-charge mass has proved to be an effective method in reducing the peak pressure in the near field. Particular local effects in the reduction have also been achieved by changing the content of mitigant (such as two-phase mixtures) or by designing special envelopes (shells) containing the mitigant.

However, the mechanisms of blast attenuation in the presence of a mitigant are not always clear. The mitigant attenuation effect may not even exhibit at a large stand-off distance, specifically, when evaluating the impulse attenuation. Moreover, the blast mitigation effect under environmental constraints (confinement) can sometimes result in enhancement in pressure in the presence of the mitigant.

The majority of blast mitigation experiments published in the literature deal with bulk mitigants surrounding a charge. The present experimental study analyses blast mitigation by both bulk mitigants and a mitigant dispersed over the explosion arena (a mist). The effect of confinement and possible pressure measurement inaccuracies due to imperfections in the gauge set-ups are discussed in the report, using modelling results obtained with a CFD code IFSAS II. A hydrocode (CTH) analysis with bulk and re-distributed mitigants confirms that the phase transformation and liquid breakdown are important issues for understanding and accurately evaluating the mitigation performance. By employing mitigants with different viscosities, the results of the present tests demonstrate the importance of the phase transformation and liquid breakdown mechanisms and show how they influence the mist formation from a bulk mitigant expanded by blast products. The results of the study indicate the necessity of further research into the influence of the two-phase mechanisms on the blast mitigation (peak overpressure attenuation) and an analysis of impulse change due to the presence of a mitigant at large stand-off distances.

Authors

A.D. Resnyansky
Weapons Systems Division

Anatoly Resnyansky obtained a MSc in Applied Mathematics and Mechanics from Novosibirsk State University (Russia) in 1979. In 1979-1995 he worked in the Lavrentyev Institute of Hydrodynamics (Russian Academy of Science) in the area of constitutive modelling for problems of high-velocity impact. Anatoly obtained a PhD in Physics and Mathematics from the Institute of Hydrodynamics in 1985. In 1996-1998 he worked in a private industry in Australia. He joined the Weapons Effects Group of the Weapons Systems Division (DSTO) in 1998. His current research interests include constitutive modelling and material characterisation at the high strain rates, ballistic testing and simulation, and theoretical and experimental analysis of the warhead processes. He has more than seventy papers published internationally in this area.

T.G. Delaney
Weapons Systems Division

Trevor Delaney began his apprenticeship in Weapons Effects Group in 2000. He obtained his Advanced Diploma in Electronic Engineering in 2005 at Regency Park TAFE. He is now working in Weapons Effects Group of Weapons Systems Division (DSTO), where he is currently providing high speed instrumentation support for short duration explosive events.

Contents

1. Introduction

Improvised explosive devices (IED) are presently a common threat to both civilians and military personnel. Therefore, methods of IED neutralisation are being investigated and analysed by Defence and university research communities. One of the most popular approaches to the problem of explosive blast is by mitigation using various shields including water and water mist. Below is a short review of recent findings in this area of study.

Attenuation of blast by bulk mitigants that are in direct contact with a High Explosive (HE) charge has been extensively studied [1]. The mitigants studied were water, glycerine, expanded mica (Perlite) (Special/Fine and Ultrafine specifications), and sand. Water was mixed with microballoons to introduce porosity resulting in average material density of ~ 0.5 g/cm^3. The study showed that Ultrafine Perlite, water containing microballoons and glycerine have approximately the same blast mitigation performance while a Special Perlite with a larger particle size had a poorer performance than these three mitigant materials. This result is in agreement with the attenuation laws of [2, 3], which link empirical and simulation data with analytical formulas that declare that blast mitigation increases in inverse proportion to the particle size and in direct proportion to the loading ratio (density of the mitigant). However, it is unclear which of the factors, namely, a lower density (the high porosity effect) or a larger particle size (the inertial or momentum transfer effect) of the Special Perlite, when compared with the Ultrafine Perlite, is actually the cause of the poor performance. Of the three mitigating materials mentioned above, plain water was found to be the worst mitigant. The best mitigant was found to be sand. Therefore, the paper [1] concluded that the mitigant's material density is an important factor. On the other hand, the heat capacity and heat of vaporisation of the mitigants was not found to be as important as their density when comparing the results for water and glycerine.

A simulation of blast mitigation in the presence of water barriers, which was conducted in study [4] using the MSC-DYTRAN code, has suggested an arrangement that is an alternative to the direct contact of a HE charge with a mitigant (water). This mitigant arrangement consists of water separated from the explosive charge by an air gap. The paper claims a stronger attenuation when an air gap is employed compared with no air gap in a spherically symmetric set-up. However, an analysis, that keeps the water mass parameter constant, was not conducted for the test arrangements considered in the paper, rather the ratio of the water thickness to the charge radius was preserved. In view of the latter preservation, the mass of mitigant for an equivalent water thickness set-up, when the water shield is spaced by an air gap, is essentially larger than for the case of a water shield in direct contact with the charge. Therefore, whether the major impact on the mitigation factor is the air gap or mass of the water is unclear. A number of 3-dimensional simulations, using the same modelling method, and a comparison of the numerical results with tests performed in a shock tube, have been conducted in [5]. The shock tube had a wider breach section, which included an explosive driver charge that was either in air or submerged in a water container (surrounded by rubber balloons filled with water). The presence of the rubber balloons was ignored in the numerical set-up, therefore, there are

discrepancies observed in [5] for a relatively small charge mass. Significant discrepancies are also observed at large stand-off distances, however, these discrepancies might be caused by the model simplification that ignores the phase transformations of and momentum transfer into the water by the detonation products during expansion. Nevertheless, the general trend observed was that the presence of water reduces the peak pressure. An influence of the water-to-charge mass ratio on the peak pressure was not described well; possible physical manifestations in the test records were effectively absorbed by the experimental scatter. A simulation conducted in paper [6] with the same physical approach but by another numerical method, has revealed an optimal water shield thickness that provided a maximum mitigation in the case of direct contact of the mitigant with the charge. Here the numerical set-up model considered a charge and mitigant that were confined in a cube bounded by solid walls. Further increases in the water thickness after the optimal value resulted in deterioration of the mitigation performance even though the mitigant mass was increased.

The same trend has been observed for blast mitigation when a charge was separated from water by an air gap. Obviously, the confinement conditions were critical in the present experimental arrangement resulting in this performance deterioration; however, the actual role of the confinement was not explored in this study. The calculations have been conducted in a small-scale set-up representing a 200 g cubic charge explosion within a 1 x 1 x 1 m cubic solid-wall box. The blast mitigation process is non-scalable; therefore, it is unclear if the conclusions [6] on the blast attenuation could be extended to distances beyond the 0.5 m range of the numerical set-up. Another small-scale simulation with MSC-DYTRAN has been conducted in [7]. This simulation has also demonstrated a reduction of the peak pressure due to the presence of a water barrier. Along with the results of study [6] previously mentioned, this study has also observed a reduction of the mitigation effect with an increase in the mass of water. This effect can also be associated with the confinement boundary conditions in the set-up [7].

Phase transformation and momentum transfer mechanisms are probably the major reason of inconsistencies in the numerical description [7] of experiments at large distances. A numerical study conducted in [8] is similar to the previous ones, using the MSC-DYTRAN code. In this case the charges are large (from 15 to 120 kg) with correspondingly large distances where the blast mitigation is analysed. In these cases [8], the numerical analysis has shown that the water thickness is a more important factor to the blast mitigation than the water mass. The measurement distances chosen in the publications [6-8] might be based on numerical reasons that force the authors to analyse small charges only at small distances and large charges at large distances. Unfortunately, the practical requirements for neutralisation of IEDs forces one to look for responses more broadly. For example, blast mitigation for charges of the order of 1kg at relatively large stand-of distances (several meters) are quite relevant. Thus, the numerical analyses mentioned above are of limited significance for the practical evaluation of the resulting blast mitigation effects.

Focusing on the multi-phase nature of water-air mixtures generated from water by the interaction of hot explosive detonation products, a numerical study of the dissipation role of aqueous foams has been considered in [9]. The major mechanism for the attenuation of the explosive blast shock wave was found to be the dissipation at the air-foam interface. It

is interesting to note that in contrast to the single-water-phase numerical analyses above, this study indicated that an increase in foam density was more effective in providing shock wave attenuation than a proportionate increase in the foam thickness. Numerical simulation [10] has been used to analyse the physical mechanisms occurring between the explosion products and water mist and the influence this has on blast wave attenuation. The study simulated a small-scale blast test in confinement. The importance of accounting for the secondary reactions in the confined conditions was noted. The numerical analysis has demonstrated that suppression of the secondary reactions had minimal effect because the water mist was pushed ahead of the shock front by the gaseous explosive products. Therefore, the primary cause of attenuation was found to be blast wave energy extraction through water vaporisation. A numerical study [11] has analysed plane shock waves propagating through a water mist. The analysis has shown that in the case of a long shock (for example, due to a long driver section of a shock tube) the stationary pressure behind the front attenuates significantly in the presence of water mist when compared with an identical stationary pressure in dry air. However, the peak overpressure at the front is higher for the case of water mist when compared with the reference pressure in the air. For a short driver section (attenuating shock waves), the peak overpressure along with the pressure behind the front was found to be unconditionally lower for the case of water mist. Unfortunately, the borderline between the overpressure increase and the overpressure reduction in mist with respect to the dry air peak overpressure was not found and a possible mechanism responsible for the transition has not yet been identified.

Presentation [12] describes a variety of blast tests exploiting the water mitigation concept. These tests were conducted in confined conditions (container, chamber, tunnel) and have generally demonstrated a reduction in peak pressure with the increase of a water mass. However, a large-scale test for simultaneous detonation of a number of shelled charges (a large underground munition storage test) has shown a pressure increase at some points when compared with the case of blast without water protection. The experimental set-up of tests conducted in [13] was a small-scale analogue of an underground munition storage facility. The test results showed that a water shield in direct contact with an explosive charge is more effective when increasing the water-to-charge mass ratio; the water mitigation effectiveness was reduced as the water was moved away from the charge. Conversely, mitigation performance was increased with decreasing charge mass while keeping the chamber volume constant. Another small-scale study has been conducted in [14] with free-field trial conditions in contrast to the previous confined trial. Here the charge was semi-spherical covered by a semi-spherical water-filled protective device. Both the charge and pressure transducers were in close proximity to the ground. This study has also demonstrated a significant effect of the ground proximity on the results (this can also be seen as an effect of confinement). A conclusion was made from these experiments that a greater attenuation can be achieved with greater amount of water in the water shield. It should be noted, however, that in that study very small charges (from 20 to 40 g in mass) and a large water-to-charge mass ratio (more than 200) have been used. Therefore, it is not clear if the conclusion can be ‘scaled’ up to explosive charges and protective shields of practical significance.

Suppression of detonation by water foams and blankets has been studied in [15] for gaseous detonating mixtures. Mainly the evaporation mechanism has been considered in

the theoretical section of this study, where the suppression was governed by the number of water droplets. The mechanism of suppression was verified with experiments, indicating a possibility of secondary explosions after injection of the foams. Use of such water foams filling an elastic shell that constitutes a mitigation device has been made in [16]. The study claims that elastic shells of a moderate compressibility (Young modulus ≤ 10 GPa) filled with plain water manifest a comparable protective effect when compared with the devices filled with aqueous foams. The mitigation performance was observed to be dependant on the ratio of the mitigation device's mass to the charge mass [16]. The mass of the mitigation device includes both the mass of the mitigant and the mass of the shell. A paper [17] based on these previous studies [15-16] has observed the influence of a number of parameters on mitigation performance that include the properties of the elastic shell enveloping a mitigant (foamed water) and the characteristics of an air gap between the device and charge. The presence of air bubbles in the mitigant is claimed to be an important factor when protecting small charges and the role of the air bubbles was observed to diminish with increasing charge size. The mitigation performance criterion included the degree of attenuation of the peak pressure and impulse. Results of this study showed that the impulses for a device in direct contact with the charge and for a device spaced from the charge by an air gap, converge with increasing distance from the point of detonation. The blast wave impulse converges to the same value that was also observed for detonation of an unprotected charge. It should be noted that the possibility of an increase in the impulse towards a target for the protected charge over that for the bare charge at large distances, is usually ignored in the literature. The results from the studies [15-17] resulted in a 'Fountain' device described in a paper [18]. This device is a set of compartments enveloped with elastic shells (the shell material is an Aramid fibre composite) that are filled with a two-phase liquid (aqueous foam). Overpressure and impulse measurements following the detonation of a 0.8 kg condensed explosive charge protected by the Fountain device have been conducted in the study [18]. According to the study, a comparison of the data for unprotected and protected blast tests has demonstrated a significant human injury protection effect with a greater than 4 times increased mitigation efficiency, if based on the charge weight equivalency criterion resulting in the same injury.

The experimental and theoretical studies listed above demonstrate a protective effect of water, water foams and other porous substances against explosive blast wave effects in many cases. This effect is obvious at relatively small distances from the charge and when the water-to-charge mass ratio is increased. Among the factors affecting mitigation performance are: i) test scale; ii) air gap between the mitigant and the explosive charge; iii) mitigant properties (specifically, its phase content and porosity); iv) environment (confinement), surrounding the charge; and v) the mitigant arrangement (shell containing the mitigant, and shell's material properties). At the same time, many influencing factors and the mitigation mechanisms are still unclear. Specifically, the impulse effect on a target at large stand-off distances and the effect of the type and composition of the mitigant are the least considered issues of the blast mitigation process.

The purpose of the present study is to conduct preliminary experimental work analysing the influence of mitigant dispersion (content/structure of the mitigant) on the blast mitigation performance.

2. Experimental Set-Up

This section describes the chamber and details of the measurement equipment that were used during the investigation of blast mitigation by water mist as conducted in the High Explosives Firing Complex (HEFC), DSTO Edinburgh. HEFC Blast chamber 1 was used, which has a maximum charge limit of 5 kg of High Explosive (HE). All charges were cylindrical, 500 g Composition B (60/40 RDX/TNT) and initiated by an Exploding Bridge Wire (EBW) detonator. A schematic of the charge and gauge lay-out (top view) is shown in the schematic of Fig. 1. The gauges have been positioned with a slight offset in order to minimise the downstream flow disturbance.

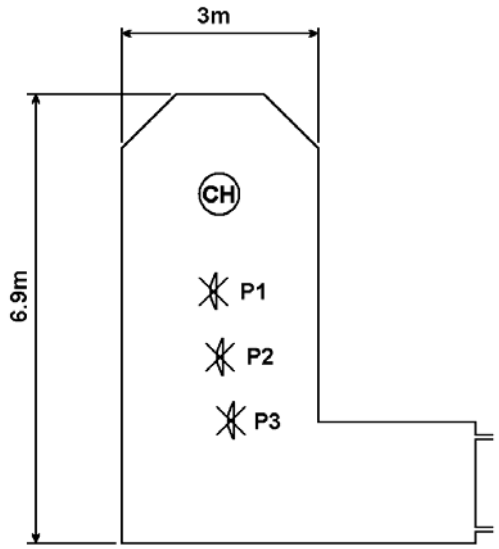

Figure 1. Schematic of a test set-up for the charge (CH) and gauges P1, P2, and P3

The pressure transducers used throughout the experiments were Endevco model 8530C-50 and 8530C-100 gauges. These are piezoresistive transducers and are rated to a maximum pressure limit of either 50 or 100 psi (350 and 700 KPa). Endevco gauges employ a silicon diaphragm onto which a four-arm Wheatstone bridge has been diffused. The gauges were mounted side-on to the direction of the blast wave, and hence measured incident static pressure. Each pressure gauge was mounted inside a machined nylon (Delrin) and O-ring mount, which in turn was screwed into the centre of a large baffle plate. The nylon mount is used in an attempt to damp high frequency vibration. A baffle plate is shown in Fig. 2. The baffle plate is a machined aluminium knife-edged disc, which is fixed to the top of a gauge stand. This plate design ensures that minimal aerodynamic flow interference is encountered in the vicinity of the gauge. The diameter of the knife-edged disk was approximately 240 mm. This arrangement can be sensitive to set-up inaccuracies therefore care must be taken to ensure the baffles are aimed correctly at the centreline of the charge being tested.

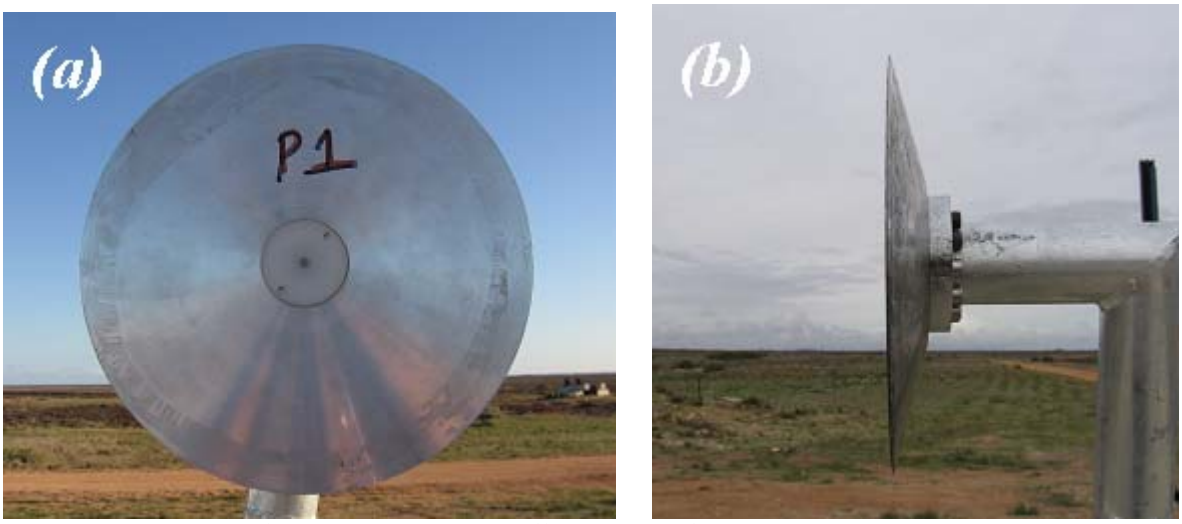

Figure 2. Close up of the pressure gauge baffle: (a) – the front view and (b) – the side view

Figure 3. Pacific 5871 3-Channel Data Recorder with 5871Command Encoder

Figure 4. Model M2-SS316 Water Mist Nozzle

Pressure data were recorded on Pacific Instruments 5800 Transducer Data recorders. Pacific Instruments data recorders are shown in Fig. 3. These feature a programmable digitising rate of up to 2 million samples per second at 14 bit resolution and have up to 4 MByte of non-volatile sample memory. At the maximum sampling rate, each channel has a maximum record length of 2 seconds. They can be powered by an external 12V supply and have been designed for operation in harsh environments. Measurements from each pressure gauge are recorded on individual channels and are then downloaded via an Ethernet connection onto a laptop computer, where the information is subsequently processed.

Fig. 4 shows the nozzles employed to create a uniform water mist field. These nozzles are commonly used in indoor fire protection sprinkler systems. Fig. 5 shows the orientation of the water nozzles for a water mist blast mitigation experiment (this is one of the test set-ups; all of the experiments will be described in detail later). Each water nozzle was separated by exactly 1 m, and located 0.5 m above the height of the charge. This nozzle spacing was identical for all tests in the present test series; this spacing was selected from the drop size distribution analysis [19] in order to keep the water concentration as homogeneous as possible at 1 m level above the ground.

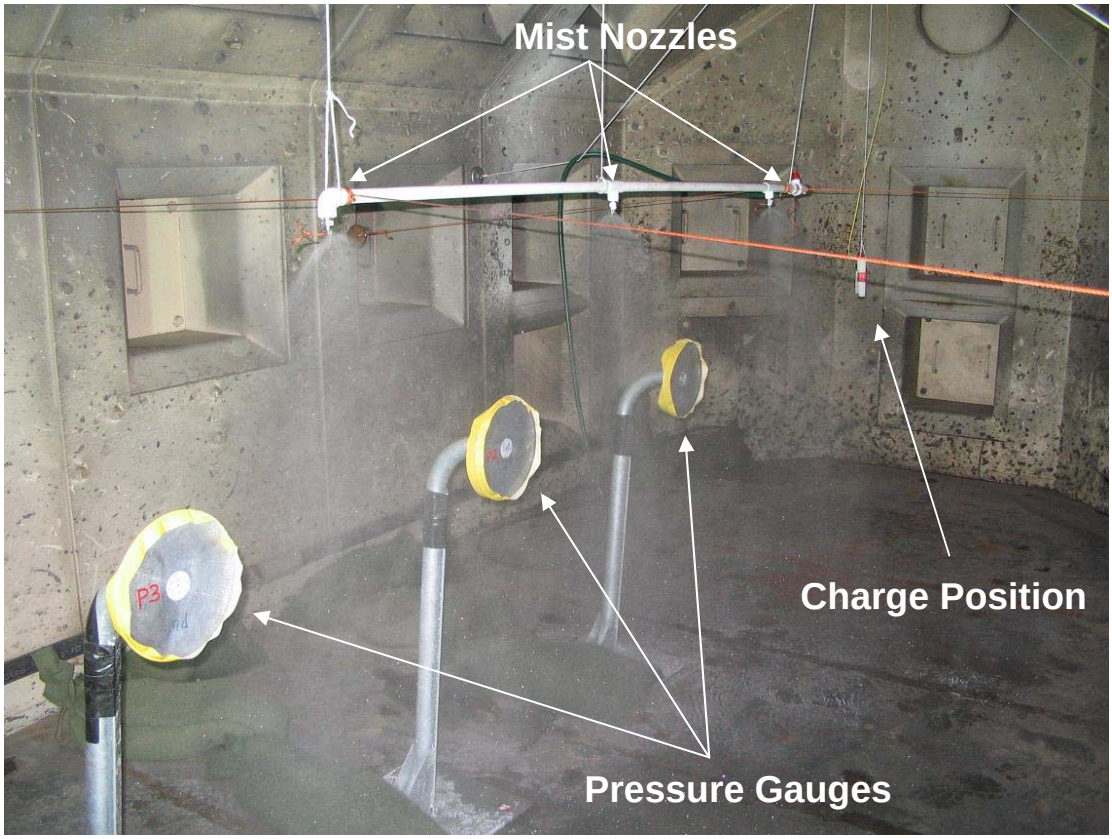

Figure 5. Experimental set-up (Set-up 3) for experiment with water mist aligned along the shock path

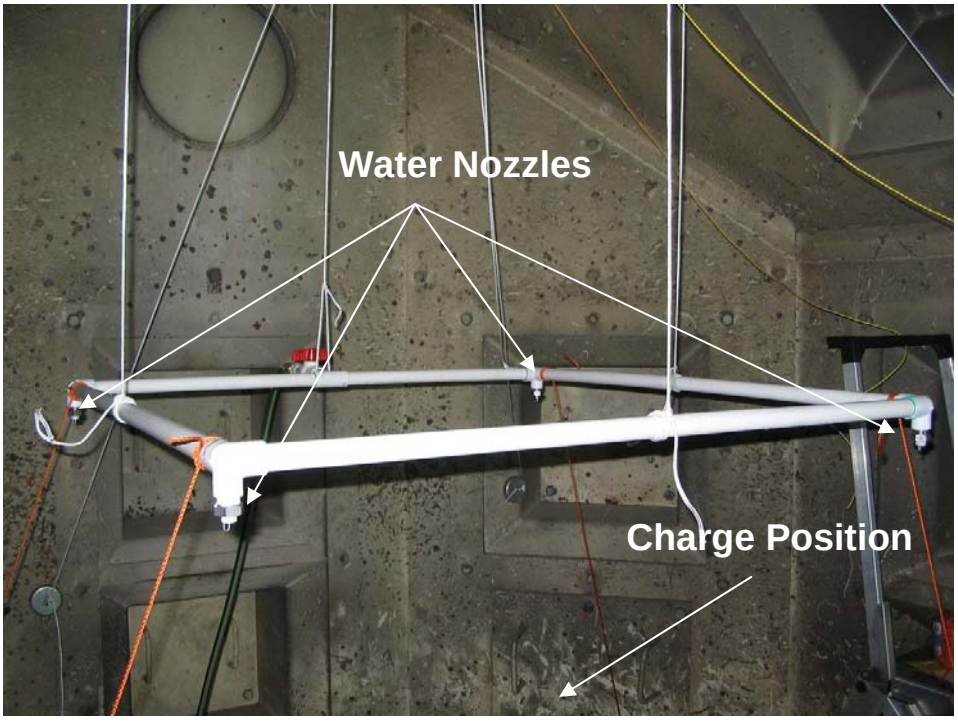

Figure 6. Experimental set-up (Set-up 2) with water mist distributed over the charge

The water flux for the present nozzle type is approximately 6 L per minute and an average droplet size is approximately 80-90 μm (in fact, distributed in the 50-100 μm range for a single nozzle [19]).

Five experimental set-ups were employed. The first set-up of the present test series was selected to provide a reference point where a bare charge is exploded and pressure data collected. The pressure gauge test arrangement for this test was as shown in Fig. 5, but with the mist sprinkler system removed from the arena.

Set-up 2 is shown in Fig. 6 and enabled the spraying of water droplets directly into the charge explosion area, thus replacing the traditional set-up of a charge submerged in water with that of a charge surrounded by a water mist. Each of the nozzles generates a quasi-homogeneous mist distribution around the area directly 0.5 m below the nozzle and 0.9 m in diameter [19]. Therefore, the 4-nozzle array in Fig. 6, with the nozzles at the corners of a 1 m square, is a practical arrangement for surrounding a charge that is 0.5 m below the centre of the square with a reasonably homogeneous water mist. Unfortunately, a perfectly homogeneous distribution is impossible to achieve when using a number of nozzles for generation of such a water mist. For example, the report [19] shows that the distribution pattern (water mist mean diameter and density of droplets) is a function of the number of nozzles involved in the sprinkler system. For a two-nozzle arrangement larger droplets have a higher chance to form in the area of spray interaction; this results in the size distribution of water droplets within the 50-150 μm range for the double nozzle system [19].

Fig. 5 shows the arrangement of water nozzles in the second water mist experiment (Set-up 3 in the present test series). In this case the water nozzles were aligned in a single line at distances of 1 m, 2 m, and 3 m from the charge and at a fixed height of 1.5 m above the ground (0.5 m above the charge). This arrangement should be sufficient to consider blast mitigation in a nearly homogeneous water mist as the shock wave propagates from the explosion point. Compared with Set-up 2, Set-up 3 involves an air gap between the charge and mitigant and a wider mitigation zone. It should be noted that the mist zone is quite non-homogeneous in the circumferential direction, when considering the set-up in a spherical coordinate system with the origin at the charge location; however, this in-homogeneity is only important at long ranges, well beyond where the gauges are mounted and only if measurements are taken in different radial directions.

Fig. 7 shows the charge set-up for experiments where the charge is submerged in a bulk liquid (Set-ups 4 and 5). A stand constructed from lengths of angle-iron was utilised to support a rubber balloon (blue sphere in Fig. 7) filled with a liquid (water for Set-up 4). A hole was cut into the top of an inflatable exercise ball in order to attach a clamp onto the ball. The ball was then suspended from the top of the stand via the clamp, and filled with approximately 110L of water. The charge was then waterproofed using a tight plastic bag, and suspended in the centre of the sphere from the chamber ceiling.

The experimental set-up for the charge submerged in glycerine (Set-up 5) remained identical to the previous event, with the exception of using 70L of glycerine rather than water. As glycerine has a higher density than water, the exercise ball did not expand at the

same rate as when it was filled with water; subsequently a lower volume of glycerine was achieved when the ball was fully filled, reaching slightly less mass than the mass of water in the previous set-up.

Figure 7. Charge set-up for tests with an explosive charge submerged in bulk liquid

Table 1 summarises the set-up arrangements for all the tests including the reference test (bare charge), two tests with the water mist mitigants, and two tests with the bulk liquid mitigants.

Table 1. Set-ups for water mitigation tests

Set-up number	Mitigant
1	N/A (bare charge)
2	Water mist (4 nozzles over the charge)
3	Water mist (3 aligned nozzles along the shock path)
4	Water (bulk liquid in a light rubber balloon)
5	Glycerine (bulk liquid in a light rubber balloon)

It should be noted that for the present test set-ups the mitigant-to-charge mass ratios are not kept constant (except for Set-ups 4 and 5). Therefore, the tests may only serve as indicators for qualitative comparison of different mist arrangements and of different properties of bulk mitigant.

3. Test Results

Results of the tests recorded by the pressure transducers are shown in Figs. 8-12 below. Indices P1, P2, and P3 in the plots correspond to records from the pressure gauges, the spatial positions of which are shown in Fig. 1.

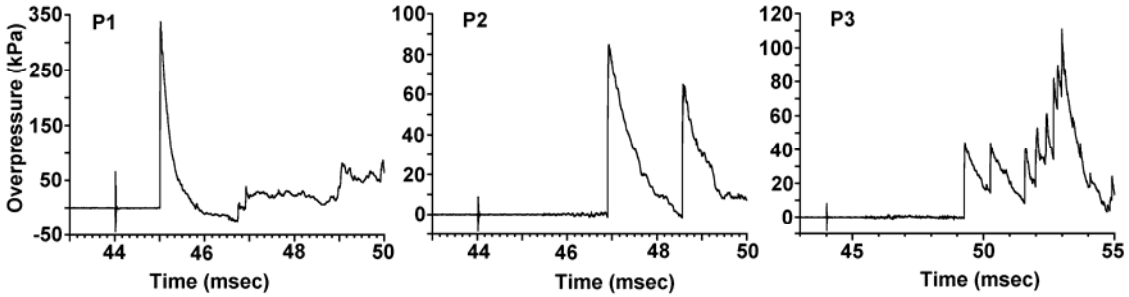

Figure 8. Experimental overpressure histories for the explosion of a bare charge (Set-up 1)

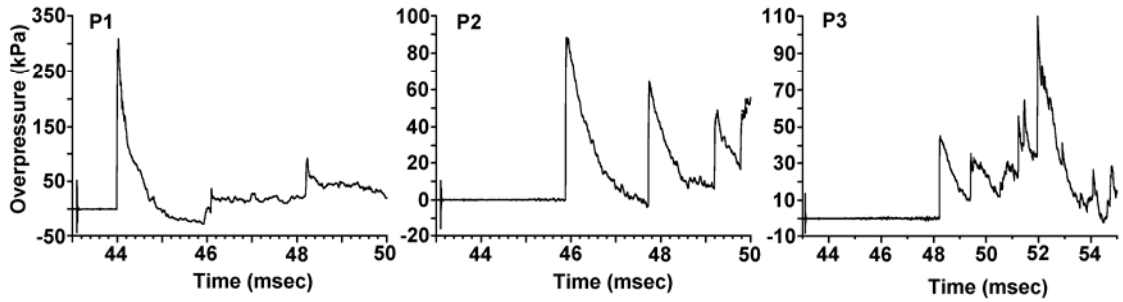

Figure 9. Experimental overpressure histories for the explosion of the charge that was directly surrounded by water mist sprayed by 4 nozzles in the square arrangement (Set-up 2)

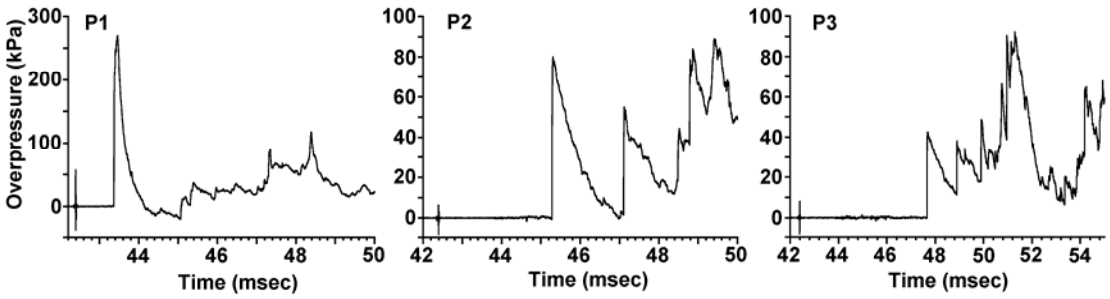

Figure 10. Experimental overpressure histories for the explosion of the charge with water mist sprayed by 3 nozzles in the line arrangement (Set-up 3)

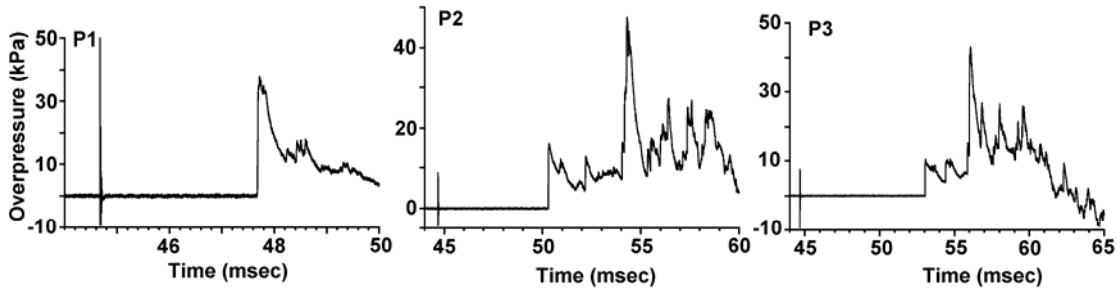

Figure 11. Experimental overpressure histories for the explosion of the charge submerged in bulk water (Set-up 4)

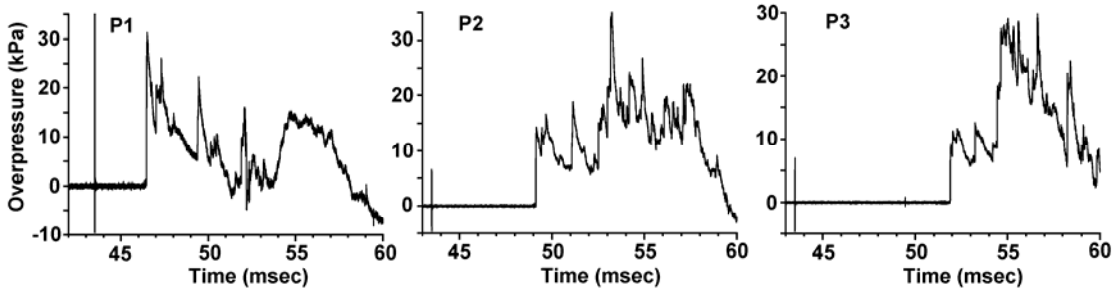

Figure 12. Experimental overpressure histories for the explosion of the charge submerged in bulk glycerine (Set-up 5)

It is seen from the test results that the overpressure pulses recorded by the pressure transducer P1 shown in the plots are similar to traditional records; however, the negative phase is not very pronounced in these records. Secondary pulses are common for these records as shown by transducer P2 and they are, in fact, relatively stronger for the explosion of charges surrounded by bulk mitigants (Figs. 11-12). It is obvious that the secondary pulses always dominate as shown in the records of transducer P3. The most alarming fact deduced from the results is that overpressure in the secondary pulses recorded by transducer P3 in Figs. 8-10 and overpressure in the secondary pulses recorded by transducers P2 and P3 in Figs. 11-12 significantly exceed the front peak pulses. Accordingly, this issue will be discussed in detail in the following section.

The peak overpressure results have been summarised for all the tests for the lead pulse in Fig. 13. This graph shows peak overpressure comparison between each event. Both the water and glycerine bulk mitigants reduced the peak overpressure by over 80% at a distance of 1.5 m in comparison to the reference charge. In contrast, the water mist had less of an effect on reducing the peak overpressure. The water mist directly over the charge in the square water nozzle arrangement (Set-up 2) reduced the peak overpressure by less than 10%, whereas the water mist in the line orientation reduced the peak overpressure by approximately 20%. This is not surprising, keeping in mind the mass of the mitigant in each case (the charge mass is constant for all the events). The mass flow rate of the water suspended in air for Set-up 2 is approximately 24 L per minute in all directions around the charge (that means approximately 3 L in the direction of shock propagation along the

gauge line). It is approximately 18 L per minute just in the single direction of the shock propagation (Set-up 3), and 10-12L of bulk liquid in the direction of shock propagation aligned with the gauge stands for Set-ups 4-5.

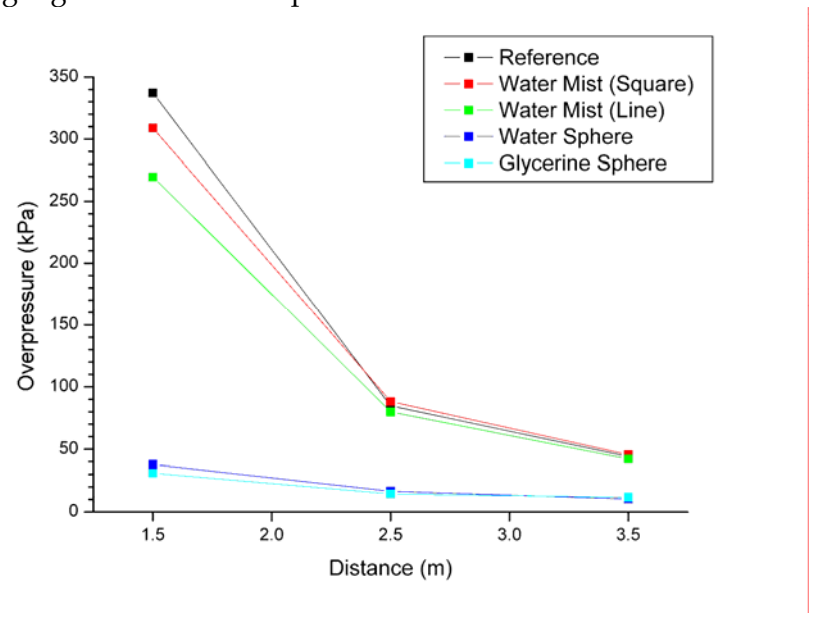

Figure 13. Peak Pressure Comparison Graph

Thus, a significant reduction of the peak pressure when changing the set-up from the bare charge to water mist and then to bulk liquid seems to be expected due to the significant increase of the water-to-charge mass ratio. The secondary pressure peak determinations, however, are not obvious and will be discussed in the next section. Similarly, the mitigation effect variation between Set-ups 2 and 3 and between Set-ups 4 and 5 is not obvious. Nevertheless, it is worth noting that enhanced mitigation is observed for the glycerine mitigant even though the mass of glycerine is slightly less than the mass of water. This leads to the conclusion that phase transformation and liquid breakdown mechanisms, which are obviously quite different for water and glycerine, are important.

4. Influence of the Chamber Confinement

In this section we will analyse the influence of the chamber confinement on the overpressure data that can be obtained in the set-ups corresponding to the records of Figs. 8-12. It is natural to associate the secondary pressure pulses in the records with the confinement influence and the present analysis considers how pivotal this influence could be. A schematic of the chamber top view shown in Fig. 1 gives a hint that the major contribution to the pressure fluctuations can be made by the lateral walls of the chamber and the floor. The door passage may have only a tertiary effect if it is found that the secondary pulses in the records are caused by the effect of the walls and the floor. Therefore, a simplified symmetrical set-up was chosen for the numerical analysis that neglected the door passage and the door end of the chamber. In this simulation the charge is placed equidistantly from the wall, floor and the ceiling at one (further) end of the

chamber represented as a rectangular solid-wall box in Fig. 14 (the origin in the coordinate system of the chamber representation in Fig. 14 is at the right further corner of the floor).

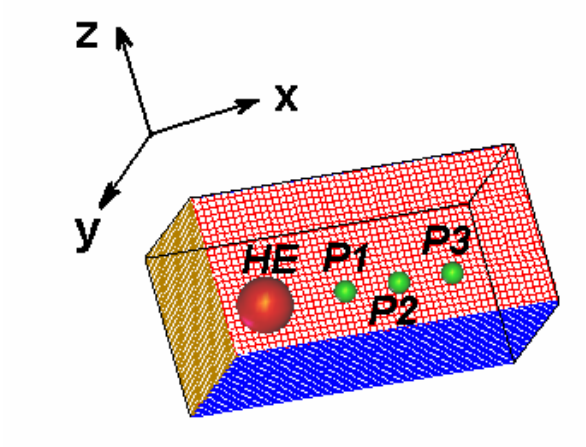

Figure 14. Test set-up for the charge (HE) and gauges P1, P2, and P3

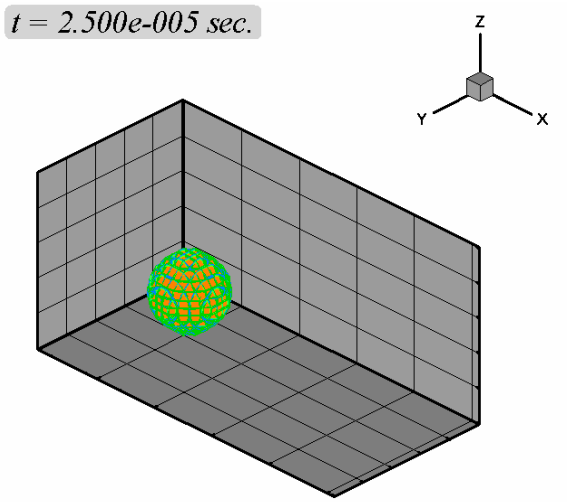

Figure 15. Pressure isosurfaces at t= 0.25 msec

Thus, the simplified set-up shown in Fig. 14 presents the chamber as a box with dimensions 6 x 3 x 3 m (in the x,y,z-coordinate space of Fig. 14 with the origin at the above mentioned corner of the box on the floor $z = 0$ at the further wall $x = 0$ intersecting the right lateral wall $y = 0$); the door end of the chamber is closest to the box end ($x = 6$ m) and the further end of the chamber ($x = 0$) is closest to the charge. The charge (denoted by HE) is placed 1.5 m away from the further end of the chamber, and the gauges (the tracing points) are placed approximately as shown in Fig. 1: the transducer P1 at point (2.5, 1.5, 1.5); P2 – at (3.5, 1.5, 1.5); and P3 – at (4.5, 1.5, 1.5). The problem was modelled with a CFD code IFSASII [20] with a 3-dimensional set-up option. The effect of blast was represented by a pre-expanded high-pressure balloon, the parameters of which have been selected such that the energy of the balloon would correspond to the energy of a 0.5 kg high explosive used in the tests.

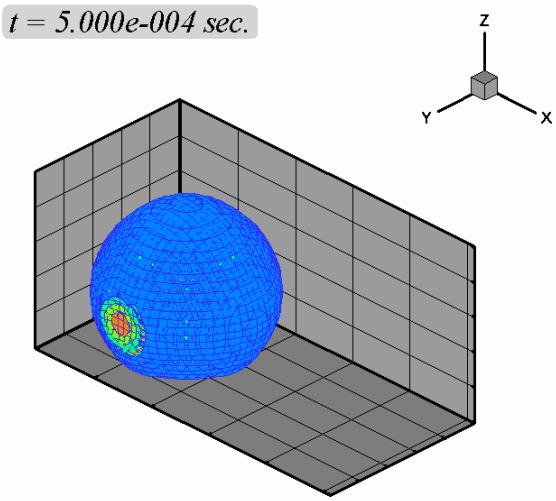

Figure 16. Pressure isosurfaces at t= 0.5 msec

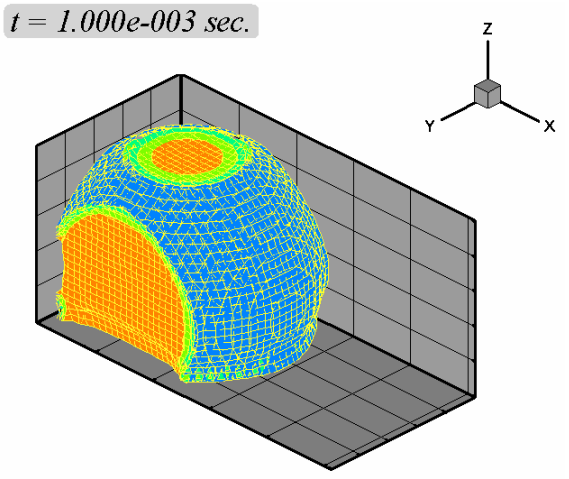

Figure 17. Pressure isosurfaces at t= 1 msec

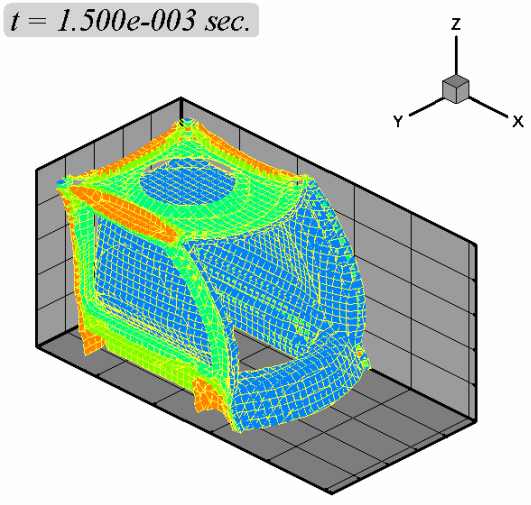

Figure 18. Pressure isosurfaces at t= 1.5 msec

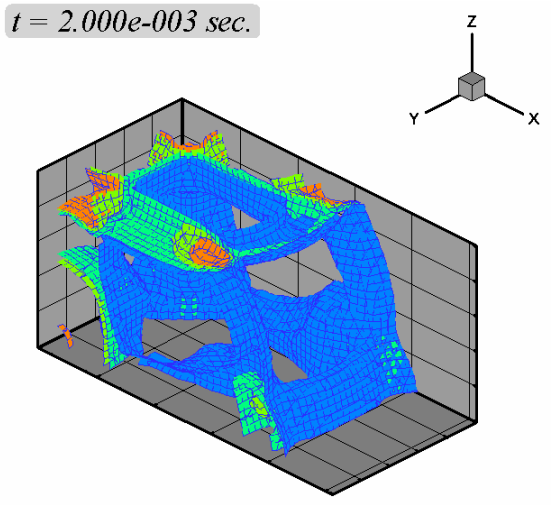

Figure 19. Pressure isosurfaces at t= 2 msec

Numerical results of the IFSASII modelling of blast wave propagation, in a medium that has properties of the air at normal conditions, are shown in Figs. 15-19; the transmitting medium (air) is described by the ideal gas equation of state with the polytropic exponent of γ = 1.4. It is seen that the shock wave reaches the chamber walls at approximately 0.5 msec after the start of the process (Fig. 16). In reality, the shock-wall interaction may happen slightly later with respect to the detonation initiation because the start of the detonation process is not considered within the present modelling set-up. This time shift is equal to the delay caused by expansion of the detonation products to the high-pressure balloon volume that is used as an initial condition in the present case. The shock reflection is well developed at 1 msec (Fig. 17), and the reflected wave definitely interacts at a time later than 1.5 msec with the shock front of the primary shock wave propagating in the x-direction (Figs. 18 and 19).

To monitor how confinement affects the simulated pressure data measurements at the points P1, P2, and P3, we have traced pressure at those points and the corresponding pressure plots versus time are drawn in Fig. 20. It is seen that the secondary pulses significantly exceed the lead pulse at the points P2 and P3 and exhibit themselves clearly in these plots. In order to separate the confinement contribution from the primary wave effect, we have calculated the same blast-gauge arrangement in the free-field conditions and the corresponding pressure profiles are drawn in Fig. 21. Comparison between the pressure profiles in Figs. 20 and 21 shows that the negative overpressure phase is significantly reduced at the point P1 under confinement conditions and it is absolutely eliminated at the point P2. At the same time, the confined and free-field predictions of the lead pressure pulses calculated at the tracing points P1 and P2 are in agreement. However, the lead pressure at tracer P3 might be affected by the confinement (there is an approximately 50% increase for the confinement set-up), even if the lead pulses arrive at the point P3 simultaneously for both set-ups and look similar to each other in Figs. 20(c) and 21 (c).

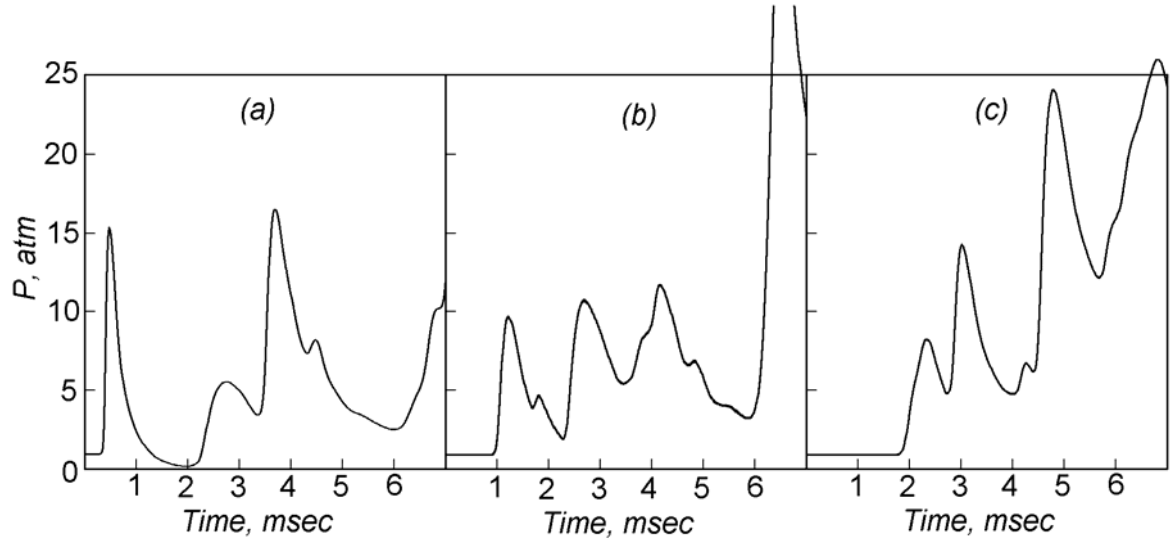

Figure 20. Overpressure profiles at the tracers P1 (plot (a)), P2 (plot (b)), and P3 (plot (c)) in the set-up of Fig. 14

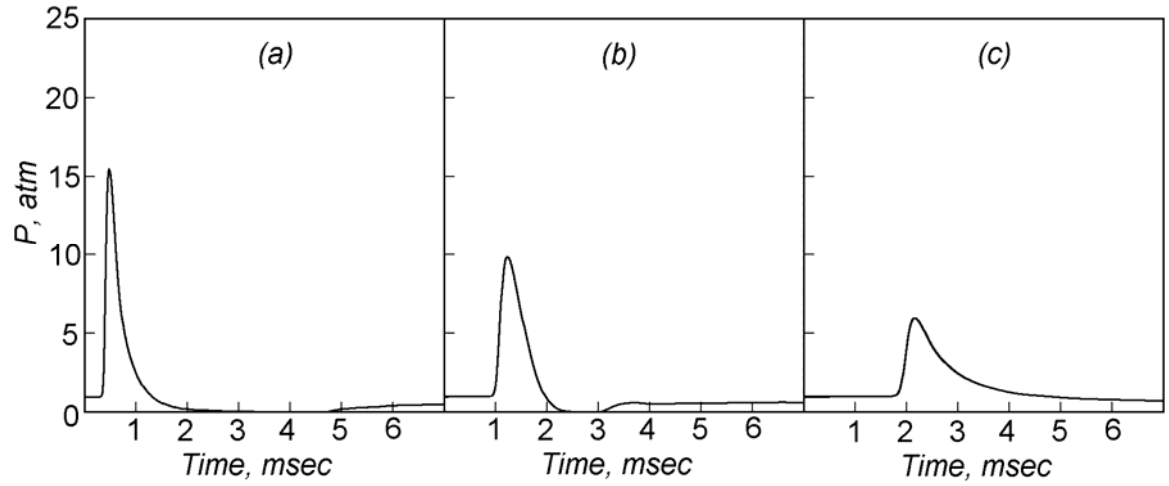

Figure 21. Overpressure profiles at the tracers P1 (plot (a)), P2 (plot (b)), and P3 (plot (c)) in the free-field conditions

It should be noted that the explosive blast products are represented very crudely with the ideal gas equation of state, an approximation that was used for the modelling described by the results shown in Figs. 20 and 21. In reality, the interaction of the explosive detonation products and, the mitigant material, cannot be described with such a simplistic equation of state. In order to gain an insight into the effect of the equation of state representation we have conducted calculations in the same two set-ups for a gas with a different heat capacity ratio $\gamma = 3.0$. This approach is frequently used for description of a lower compressibility of the blast transmitting medium.

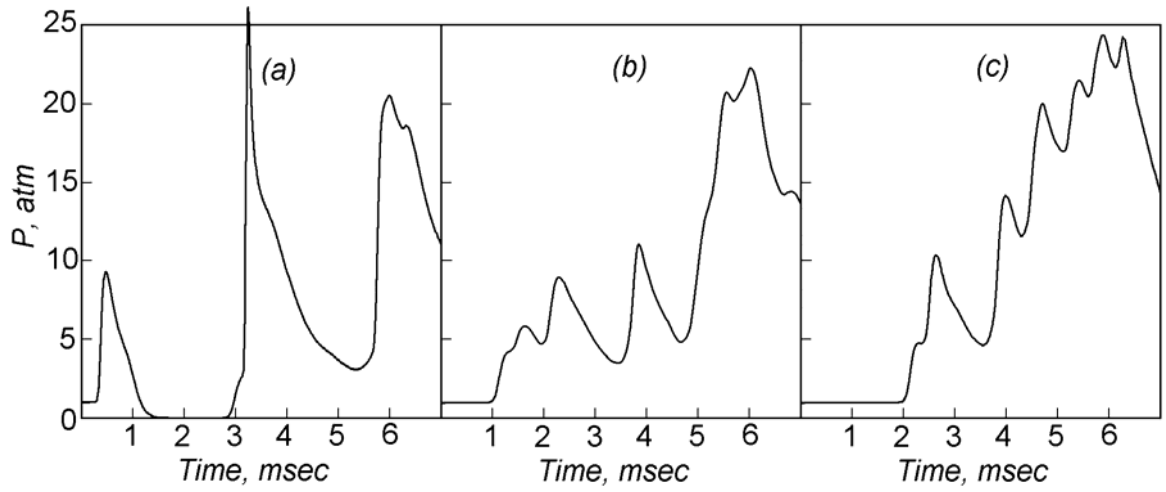

Figure 22. Overpressure profiles at the tracers P1 (plot (a)), P2 (plot (b)), and P3 (plot (c)) in the set-up of Fig. 14 for a low compressible blast-transmitting gas

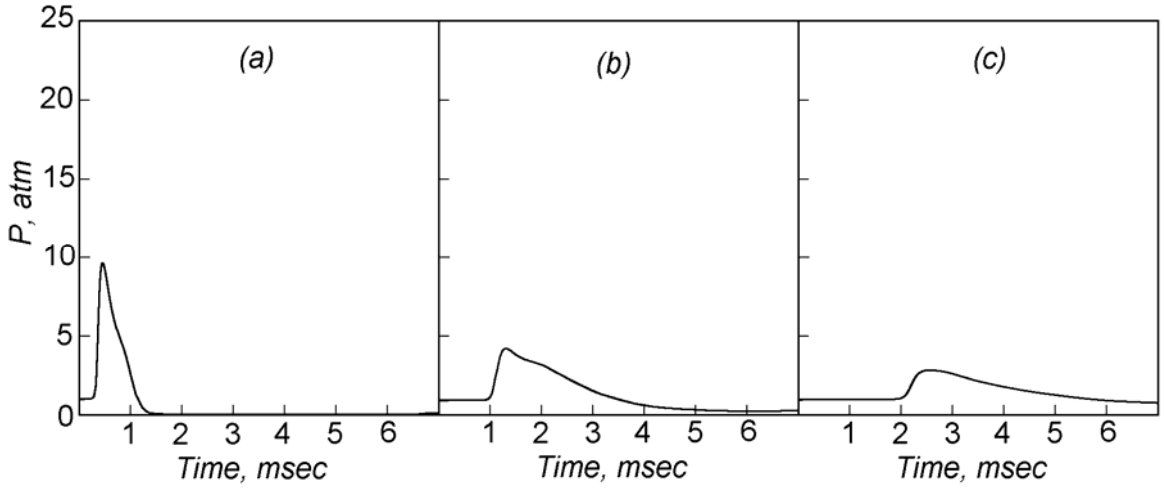

Figure 23. Overpressure profiles at the tracers P1 (plot (a)), P2 (plot (b)), and P3 (plot (c)) in the free-field conditions for a low compressible blast-transmitting gas

Corresponding numerical results are shown in Figs. 22 and 23. Comparison between the results demonstrates that the medium compressibility may significantly affect the peak pressure at late times. As is seen from the comparison of the lead peak pressures in Figs. 22(b) and 23(b), the lead overpressure may start to be affected by the confinement at 1 msec even though the secondary pressure pulses are reduced as a consequence of the equation of state modification. Nevertheless, it is expected that the peak pressure recorded at P1 may closely correspond to the peak pressure observed in free-field conditions. It should be noted that the description of the transmitting medium with the ideal gas equation of state at a constant exponent, even when modifying the heat capacity ratio, is still highly inaccurate for such a complex multi-phase environment. However, the use of such an approximation allows us to evaluate the validity of extrapolating from the present pressure measurements to the free-field conditions.

5. Influence of the Pressure Gauge Set-Up

This section analyses the influence of gauge set-up on the pressure measurements. As Fig. 2 shows, a pressure transducer is embedded into a gauge baffle. The gauge baffle is designed to protect an expensive transducer from the harsh environment where the gauge operates. In order to minimise the dynamic component of pressure, when recording the data, the pressure baffle is oriented by the baffle edge, facing the flow recorded by the gauge, i.e. the gauge is oriented normally to the gas flow. This orientation presumes that the velocity vector is aligned with the edge direction for such a baffle orientation. In this case the normal velocity to the baffle plane is ideally zero, so the dynamic pressure component could be neglected. In this section we evaluate contributions of the baffle orientation misalignment to the flow and the flow non-equilibrium to the pressure data. When recording physical parameters in experiments, it is usually expected that an error in the measurement set-up or in the physical conditions causes the same order of magnitude in data error to be recorded.

In order to understand if this correspondence really takes place for the gauge set-up shown in Fig. 2, we calculate gas flow in the vicinity of a similar two-dimensional configuration. The results will give us an upper bound (the worst scenario) of the three-dimensional prototype. For simplification we consider a set-up shown in Fig. 24 with the edge length of 400 mm. The gauge stand dimensions in Fig. 24 are proportional to those for the side view of the real gauge baffle shown in Fig. 2. It should be noted that for the ideal gas equation of state used in the present calculations the mathematical solutions of the Euler model equations are scalable with the scalability coefficient less than 2 in the present case. Therefore, conclusions drawn from the present simulations for the disturbance analysis should be valid.

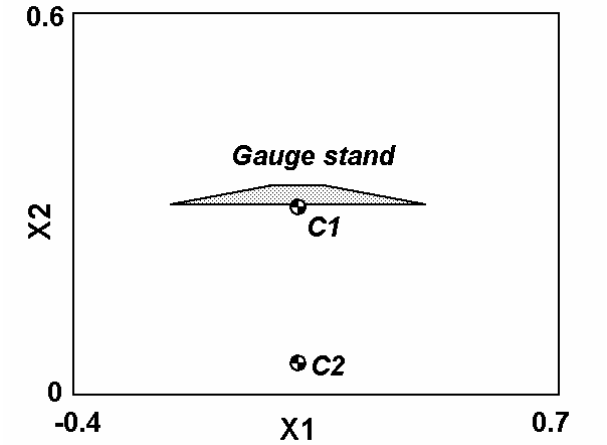

Figure 24. Schematic of the pressure gauge baffle set-up (the coordinate units are in metres). C1 and C2 are the tracing points corresponding to the position of a pressure transducer in the baffle and a position in the undisturbed flow, respectively

Referring to the schematic of Fig. 24, we set an inflow state at the left boundary $x1 = -0.4$. We considered several inflow states that correspond to an equilibrium and non-equilibrium flow. As has been mentioned, in the present modelling we consider only an

approximation of the ideal gas for the flow medium. In the present case this is probably a good approximation because the gauges operate quite distant from the explosion initiation point. To conduct the modelling we again employ the CFD code IFSASII in the present case.

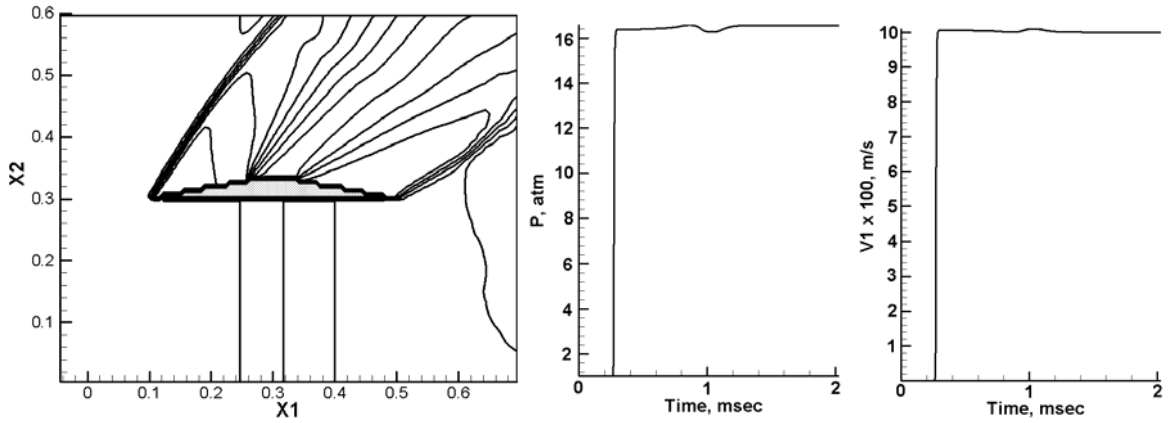

Figure 25. Modelling results for the inflow state U_i = 1000 m/s; P_i = 16.36 atm; V_i = 0 m/s. Pressure P and U-velocity at the tracer C1

For the purpose of the present study we select two equilibrium inflow states that are lying on Hugoniots in the pressure-volume space. First state (high-pressure equilibrium inflow state) might be found in a near proximity to the blast event, which is characterised by significant kinetic and internal energies, having the parameters of the absolute velocity of the flow at approximately 1000 m/s and static pressure of 16.36 atm; we denote the first state parameters as P_1^S = 16.36 atm and U_1^S = 1000 m/s. Results of the modelling with such an inflow state are shown in Fig. 25. The first plot in Fig. 25 shows the pressure contours at 1 msec after the start of inflow (the medium surrounding the baffle is initially at rest). It can be seen that when the incoming flow is strictly parallel to the gauge baffle (in the present numerical set-up, the vertical component of the inflow velocity V_i = 0), the parameters of pressure P and the horizontal component of the flow velocity (U-velocity) equilibrate very quickly in near proximity to the baffle. Therefore, the gauge baffle has practically no effect on the simulated pressure record in this case.

The following two calculations have been conducted in order to study the effect of possible gauge set-up misalignment. We achieve the misalignment by introduction of a 5% vertical velocity disturbance in the inflow. This disturbance means that the vertical velocity (V-component of the flow velocity) is varied by 5% of the total velocity of 1000 m/s, i.e. V_i is equal to 50 m/s. Physically this variation means that the flow is rotated approximately 5% off the line that is parallel to the gauge baffle plane. Geometrically this variation can be achieved when the baffle plane is rotated clockwise or anti-clockwise approximately 3˚ with respect to the flow direction.

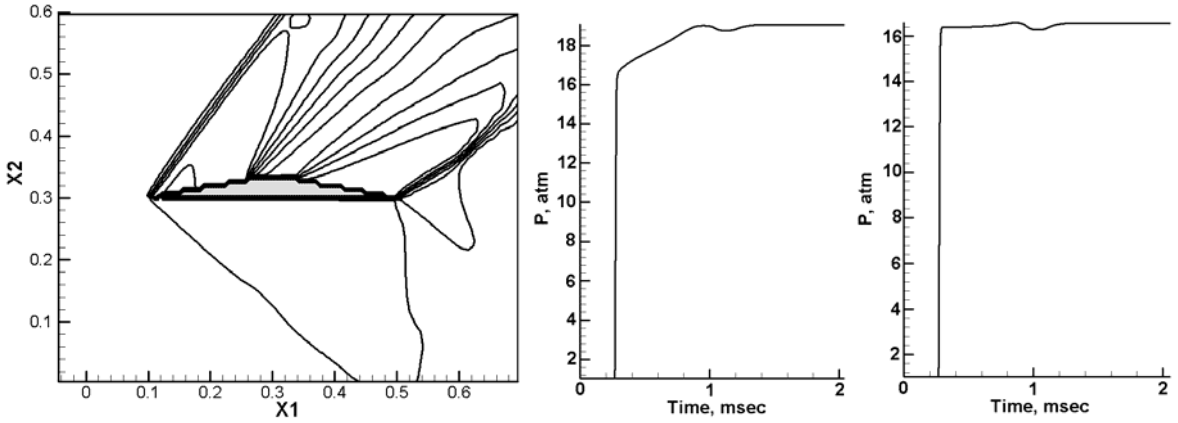

Figure 26. Modelling results for the inflow state U_i = 1000 m/s; P_i = 16.36 atm; V_i = 50 m/s. Pressure P at the tracers C1 and C2 (see Fig. 24 for the arrangement of the tracers)

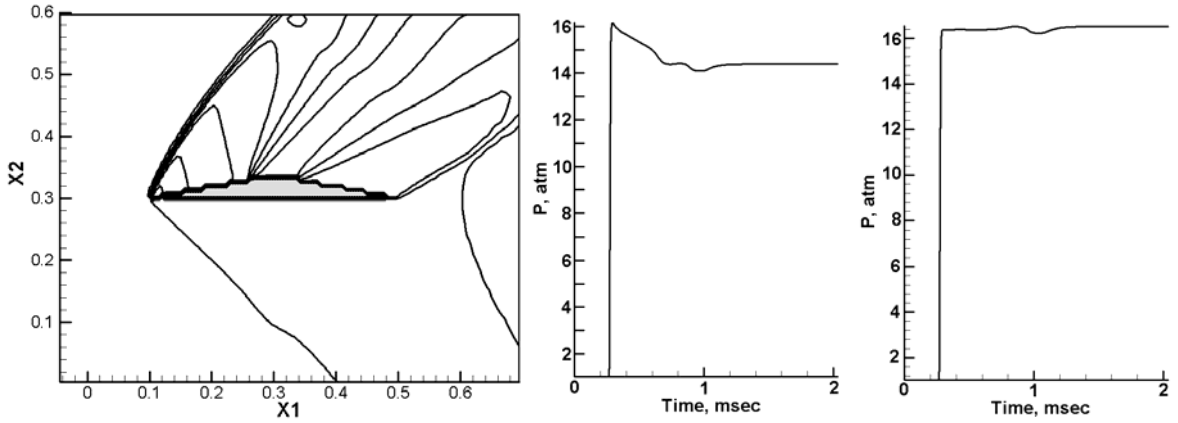

Figure 27. Modelling results for the inflow state U_i = 1000 m/s; P_i = 16.36 atm; V_i = –50 m/s. Pressure P at the tracers C1 and C2

Results of the simulations with the inflow impacting the front or back of the baffle plate at the 3° attack angle are shown in Figs. 26 and 27, respectively. The present flow-baffle configuration, when compared with the previous case, indicates that the previous flow direction is rotated 3° anti-clockwise with respect to the baffle plate or, equivalently, the baffle set-up is rotated 3° clockwise. It should be noted that formally the boundary condition had to be set at $x2 = 0$ for the case of Fig. 26 and at the boundary $x2 = 0.6$ for the case of Fig. 27, because some part of the gas in the flow is transferred from the areas adjacent to those boundaries too; however, as the evolution of the parameters at the tracer position C2 has demonstrated, these settings can be ignored because they introduce negligible flow disturbances.

Fig. 26 (the pressure isolines in the first drawing at 1 msec after the inflow) shows that when the inflow faces the baffle plate the result is a quasi-stationary oblique shock wave attached to the baffle edge; the pressure profile at C1 confirms this. Comparison of this profile with the inflow parameters observed at C2 in Fig. 26 shows that pressure increases after an equilibration time of the order of 0.5 msec to a higher level. Considering this

pressure increase as an error introduced by the baffle misalignment, the error value can be assessed, when compared with the inflow characteristics, as approximately 2/16.4 x 100% ≈ 12%. A similar outcome is observed in Fig. 27 for the misalignment in opposite direction resulting in a rarefaction flow attached to the baffle edge and in the pressure error due to the misalignment of approximately the same order. Thus, in the present case, the 5% geometrical misalignment results in the 12% pressure error.

We choose a second inflow state (low-pressure equilibrium inflow state) from the area that is far away from the blast. This state should have significantly smaller kinetic and internal energies; as an example, we take the absolute velocity of the flow at approximately 180 m/s and static pressure of 2 atm, denoting them as P_2^S = 2 atm and U_2^S = 180 m/s.

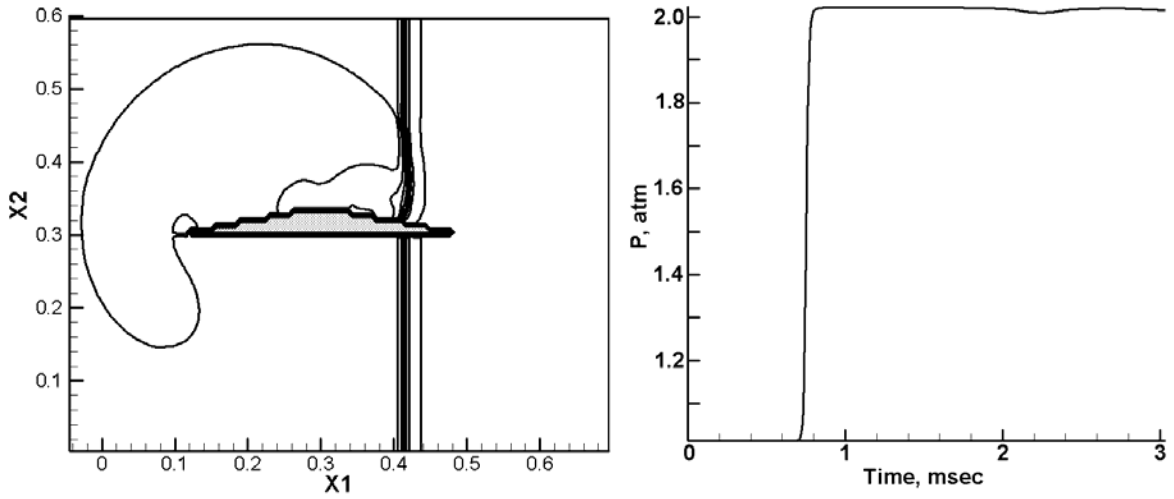

Figure 28. Modelling results for the inflow state U_i = 180 m/s; P_i = 2 atm; V_i = 0 m/s. Pressure P at the tracer C1

Results of the calculation with such inflow parameters and when the inflow is aligned with the baffle plate are shown in Fig. 28. It should be noted that the 3 msec timeframe was necessary to ensure that the flow passes over the baffle plate and therefore observe a small disturbance at approximately 2.4 msec. However, this pressure disequilibrium is negligible in the present case as the pressure profile at the location C1 (the transducer position) shows (see Fig. 28, second drawing). This larger timescale is used for the present case because the flow process is generally slower and the timescale is larger for the lower pressure conditions; it can also be seen by the position of the wave (pressure contour concentration) at 1 msec in Fig. 28 (the left picture). The major feature of the present results, when compared with the previous calculation in Fig. 25, is the presence of a detached shock as seen in the first drawing in Fig. 28.

Similarly to the previous case we can introduce a 5% misalignment (5% vertical velocity disturbance) for the present inflow state. This misalignment corresponds to a 9 m/s variation for the V-component velocity. Results of the calculation with these misalignments for the low-pressure equilibrium inflow state are shown in Figs. 29 and 30. For the case of the inflow facing the gauge baffle (the previous aligned flow direction is

rotated 3° anti-clockwise with respect to the baffle plate), the shock strength is quite weak and the misalignment does not introduce a significant disturbance in the pressure profile that is to be recorded by a gauge at the point C1 (second drawing in Fig. 29). In the case of the flow resulting in a rarefaction wave when interacting with the front edge of the baffle (the opposite orientation of the inflow in the $x2$-direction), the pressure reduction with respect to the 2 atm inflow pressure is likely to be less than 5% as seen from the pressure profile at the point C1 in Fig. 30.

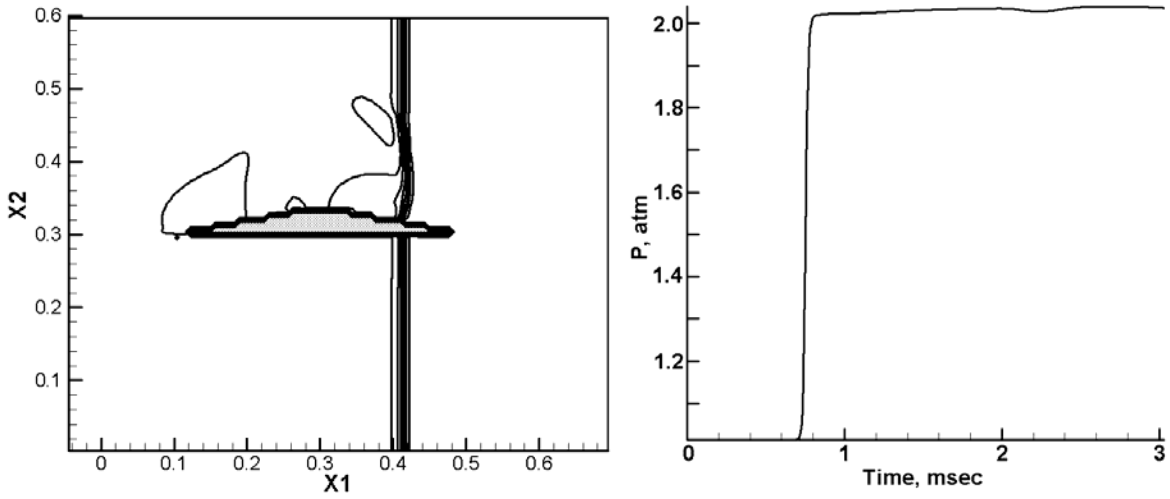

Figure 29. Modelling results for the inflow state U_i = 180 m/s; P_i = 2 atm; V_i = 9 m/s. Pressure P at the tracer C1

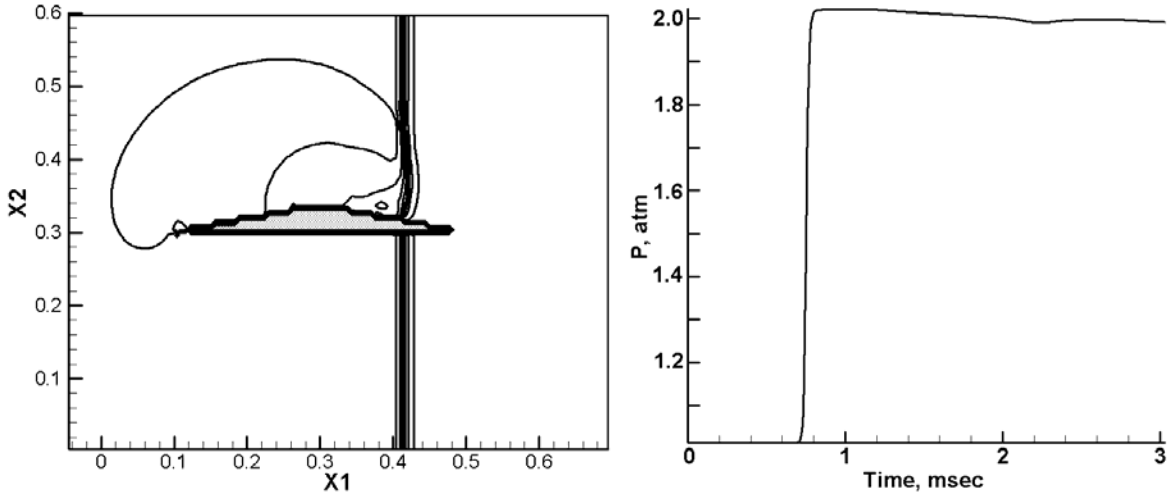

Figure 30. Modelling results for the inflow state U_i = 180 m/s; P_i = 2 atm; V_i = –9 m/s. Pressure P at the tracer C1

Thus, the ratio of the pressure disturbance (to be treated as a pressure record error) due to the gauge baffle misalignment to the inflow pressure is essentially less for the case of the

low-pressure equilibrium inflow state when compared with the high-pressure equilibrium inflow state.

In cases when the inflow state is not on a Hugoniot there is a non-equilibrium transition region where thermodynamic and kinematic states adjust to an equilibrium state. The schematic in Fig. 31(a) shows two equilibrium states (denoted by Points *1* and *2* in Fig. 31) that were used in the previous calculations (the low-pressure equilibrium inflow state with parameters P_2^S and U_2^S and the high-pressure equilibrium inflow state with parameters P_1^S and U_1^S). These states are characterised by the adjustment between the state parameters such that they are thermodynamically in equilibrium. It means that those states are from the locus of a shock adiabat A_R describing states behind the front of a right-going shock wave (when compared with the Hugoniot that describes the shock transitions in the pressure volume reference system, the shock adiabat is drawn in the pressure-velocity system and describes both the shock and rarefaction transitions).

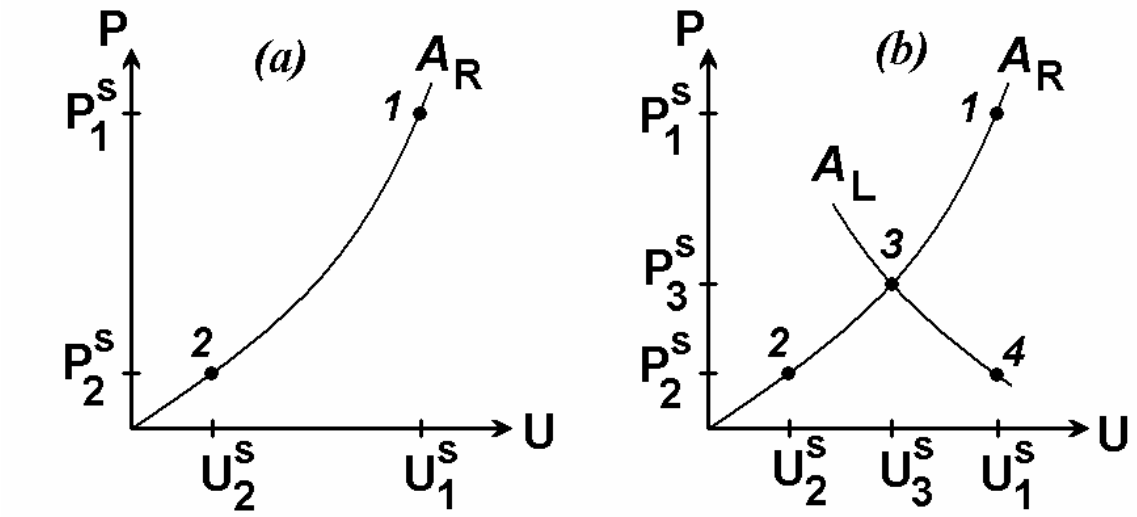

Figure 31. The shock adiabats describing the inflow states in the modelling examples of the present section

As an example of non-equilibrium state we choose the inflow state with the kinematic state from the first case considered above ($U= U_1^S$) and the thermodynamic state from the second case ($P= P_1^S$); this state is denoted by point *4* in Fig. 31(b). It is seen that in this case the flow behind the shock with such parameters behind the front cannot be reached by the adiabat A_R, therefore, it is not in the equilibrium and can be reached only after an additional transition A_L. It means that there is an intermediate state described by point *3* in Fig. 31(b) that connects the initial state (the origin) with the state *4*. The first transition is shock wave transmitting the still medium into state *3* with parameters P_3^S and U_3^S behind the shock front and the second transition is a rarefaction wave connecting states *3* and *4*.

Results of the modelling show the transition zones in Figs. 32 and 33. The first pressure contour concentration zone (left plot in Fig. 32 at t = 0.5 msec) characterises the transition from the still medium (the origin in the shock diagrams of Fig. 31) to the intermediate state (point *3*) and the second pressure contour concentration zone characterises the second

transition from the state *3* to the state *4*. This transition is clearly seen in the time history diagram in Fig. 33. It confirms that the intermediate state *3* is actually characterised by higher pressure and lower velocity. As a result, pressure and velocity after these two transitions (shock wave followed by rarefaction wave) take values (the state *4*) that are set for the inflow. It should be mentioned that in the present example the gauge baffle plate is aligned with the inflow direction.

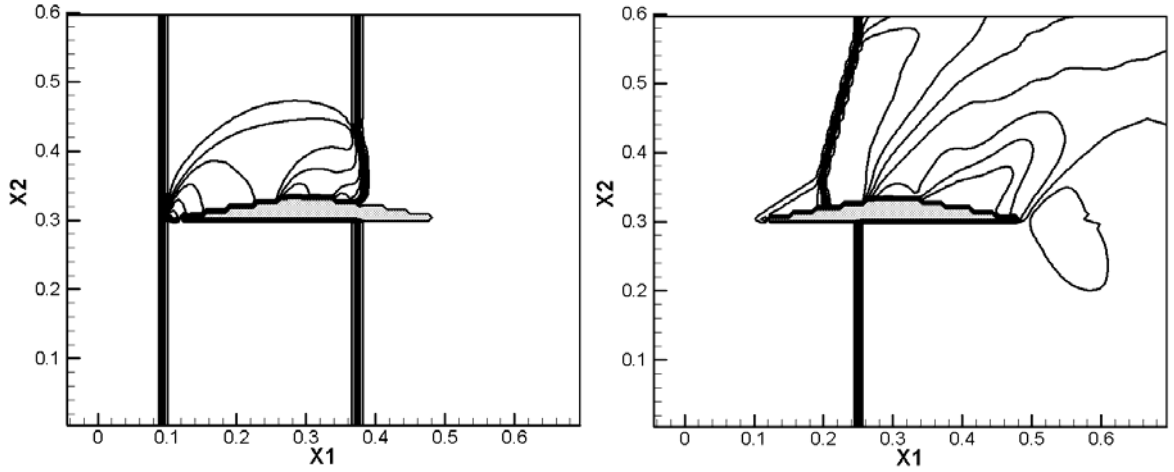

Figure 32. Modelling results for the inflow state U_i = 1000 m/s; P_i = 2 atm; V_i = 0 m/s. Pressure isolines at 0.5 (left) and 1 msec (right)

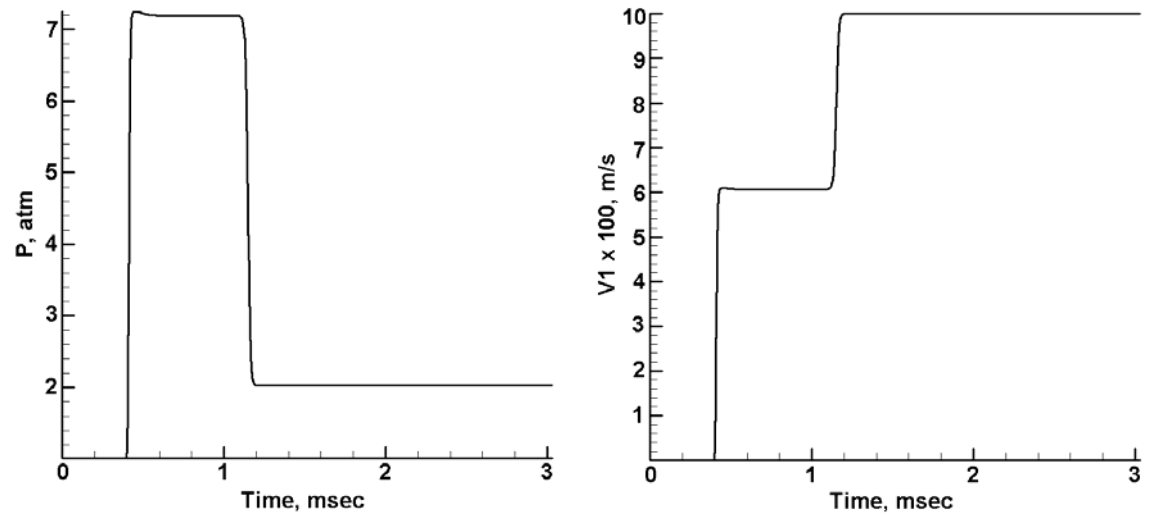

Figure 33. Modelling results for the inflow state U_i = 1000 m/s; P_i = 2 atm; V_i = 0 m/s. Pressure P and U-velocity at the tracer C1

The following two runs repeat the same 5% misalignment set-ups that were considered in the previous examples. In these cases the transition zones exhibit similar features in principle. At the tracer C2 the pressure level of the state *4* does not manifest sensitivity to the misalignments (so the final pressure level is almost coincident with the inflow pressure

of 2 atm) as seen from the results in Figs. 34 and 35 (third plots of the figures). These pressure results are fairly close to those in Fig. 31.

At the same time, at the tracer C1 parameters of the final state after the chain of transitions are quite divergent to the states recorded at C2. For the both types of misalignments, namely, the gauge baffle facing the inflow (Fig. 34) and the rear of the gauge baffle facing the inflow (Fig. 35), the final pressure recorded at C1 differs from the 2 atm of the inflow pressure by approximately 0.4 atm that gives an apparent error associated with the 5% misalignment of the order $0.4/2 \times 100\% \approx 20\%$.

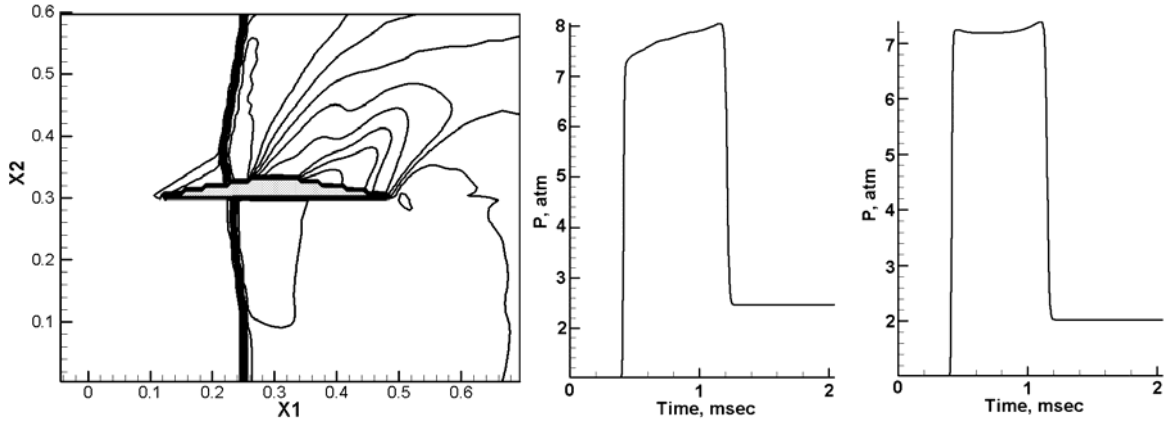

Figure 34. Modelling results for the inflow state U_i = 1000 m/s; P_i = 2 atm; V_i = 50 m/s. Pressure P at the tracers C1 and C2

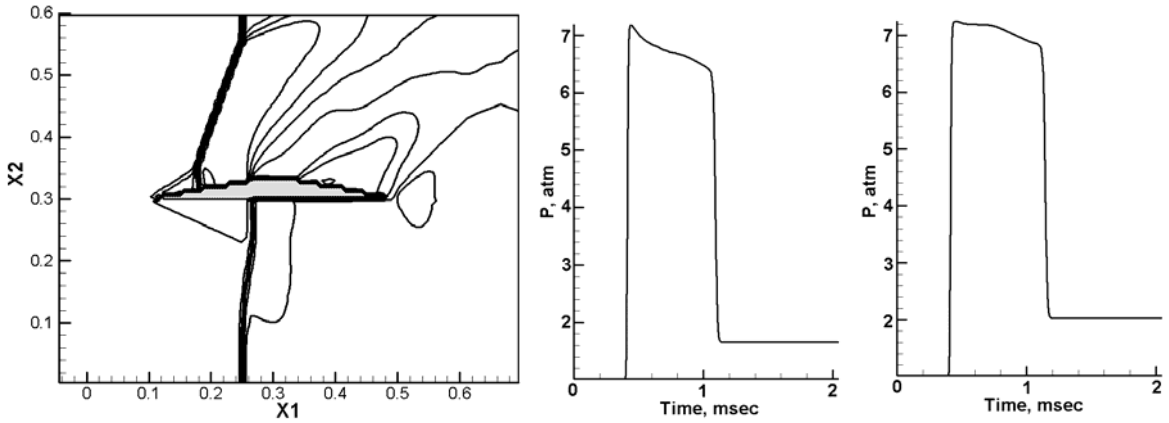

Figure 35. Modelling results for the inflow state U_i = 1000 m/s; P_i = 2 atm; V_i = –50 m/s. Pressure P at the tracers C1 and C2

Thus, in the case of non-equilibrium transition that involves an energetic (high-pressure or high-velocity) state representing the inflow, the apparent error due to the baffle misalignment is even more significant when compared with the equilibrium state.

Summarising the results of this section, the pressure measurements conducted for low-pressure states in equilibrium are the least sensitive to the gauge baffle misalignments.

High-pressure equilibrium states essentially increase the chances of the apparent error due to the misalignments, and non-equilibrium inflow states almost double the error.

6. Mitigation Governed by Water Distribution

The studies [4-8] that considered various water mitigation arrangements have usually analysed either a constant water-to-charge mass ratio or a constant water mitigant width. Major well-known mechanisms that absorb the energy of an explosive surrounded by a liquid mitigant are related to the phase transformation (evaporation of the mitigant), water breakdown (pulverisation of the mitigant), and water deformation (seen as expansion of the mitigant). Phase transformation and water breakdown mechanisms are, however, controlled by the mass of the mitigant, while the water deformation is more sensitive to the mitigant's thickness. Therefore, when a study controls only one of the set-up parameters, it is not easy to associate mitigation performance with a single mechanism (other mechanisms may be affected by parameters that are uncontrolled). The test results, unfortunately, cannot usually separate the mechanisms because they are seen as the mitigation performance curves (overpressure or impulse versus time or distance). In this section, within the single-phase approach that was also used in the abovementioned publications, we consider the influence of both factors (mitigant's mass and width) within a single problem consideration.

Table 2. Set-ups for the water mitigation simulation

	Space distribution of materials (cm)					Water-to-charge ratios	
Set-up#	HE	Air	Water		Air	α	β
1	0 – 4.1	–	–		4.1 – 300	–	–
2	0 – 4.1	–	4.1 – 12.3		12.3 – 300	26	2
3	0 – 4.1	4.1 – 8.2	8.2 – 16.4		16.4 – 300	56	2
4	0 – 4.1	–	4.1 – 15.78		15.78 – 300	56	2.85
5	0 – 4.1	4.1 – 12.3	12.3 – 20.5		20.5 – 300	98	2
6	0 – 4.1	4.1 – 8.2	8.2 – 13.3		13.3 – 300	26	1.25
7	0 – 4.1	4.1 – 12.3	12.3 – 15.4		15.4 – 300	26	0.75
		Air	Water	Air	Water		
8	0 – 4.1	4.1–11.8	11.8–12.8	12.8 – 20.6	20.6 – 21.6	21.6 – 300	26	0.49
9	0 – 4.1	4.1 – 7.9	7.9 – 9.9	9.9 – 13.8	13.8 – 15.8	15.8 – 300	26	0.98

We employ the CTH hydrocode [21] to conduct simulations in the present section. One-dimensional spherical symmetry analysis is assumed with the space distributions of energetic, mitigating and ambient materials shown in Table 2. Nine set-ups have been considered. The ratios stated in Table 2 are the water-to-charge mass ratio $\alpha = W_W/W_{HE}$ and the water thickness-to charge radius ratio $\beta = R_W/R_{HE}$. The detonation point is coincident with the origin ($R = 0$); the HE space distribution shown in the Table 2

corresponds to a 0.5 kg-charge of the Composition B HE. This explosive was modelled using the explosive burn model of CTH in the spherical symmetry set-up.

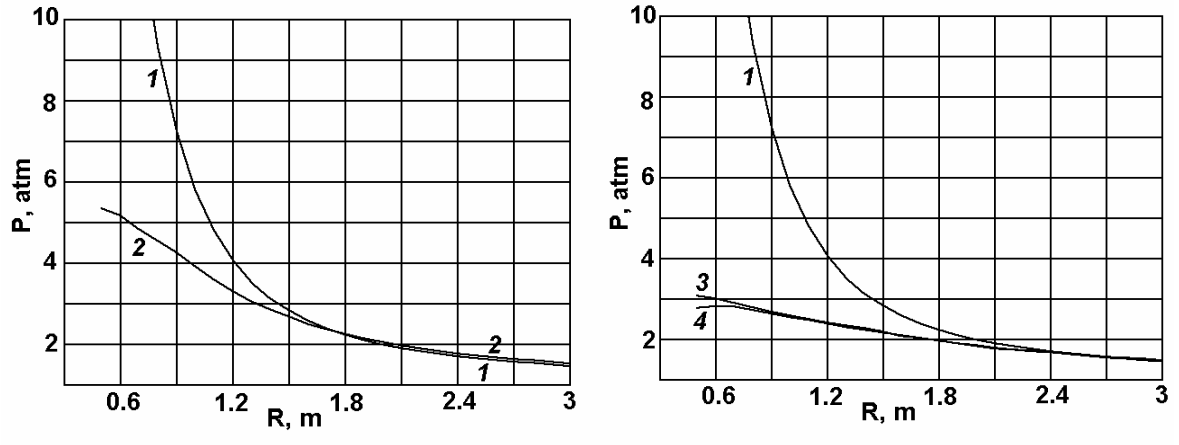

Figure 36. Comparison between the mitigation curve for explosion of a bare charge represented by Set-up 1 and that for an explosion of a charge surrounded either by water (Set-ups 2 and 4) or by an air-water sandwich (Set-up 3); see Table 2 for the set-up references

The results of the simulations are summarised in Figs. 36-39 and they are presented as a series of the blast mitigation curves (the peak overpressure versus distance from the initiation point).

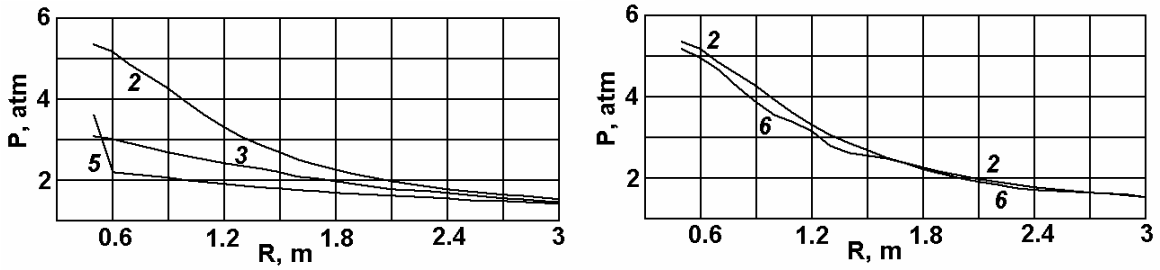

Figure 37. Comparison between the mitigation curve for explosion of a charge in direct contact with water (Set-up 2) and that for an explosion of a charge surrounded by air-water sandwiches (Set-ups 3, 5, and 6). Calculations with the Set-ups 2, 3, and 5 keep water thickness constant. Calculations with the Set-ups 2 and 6 keep water mass constant

The comparisons shown in Fig. 36 between the pressure attenuation curves for the bare charge explosion (mitigation curve 1) and for the charge in direct contact with water (curve 2) demonstrates that the charge in contact with the water, while having better attenuation performance in the close-in range, may have a slightly worse performance at a large stand-off distance. A further increase of the water mass for Set-up 3, while keeping the same water thickness as for Set-up 2, increases the attenuation performance at a large stand-off distance to the same level as for the bare charge (see comparison of curve 3 with curve 1 in Fig. 36). It should be noted that, in order to keep the water thickness constant, an air gap between the water mitigant and charge had to be introduced for Set-up 3. However, the air gap is not a cause of the performance enhancement; this is proved by the

calculation in Set-up 4 where the charge is in direct contact with the water and the water mass is the same as in Set-up 3. Comparison between curves 3 and 4 in Fig. 36 shows that the actual reason for the performance enhancement in case 3 is the mass of water. A further increase of the water mass improves mainly the close-in performance as shown in the comparison between curves 2, 3, and 5 in Fig. 37. Introducing an air gap, while keeping the water mass constant, first slightly improves the performance (see comparison of curves 2 and 6 in Fig. 37) but then results in an inconsistent behaviour, with further increases in the air gap, as shown in the comparison between curves 6 and 7 in Fig. 38.

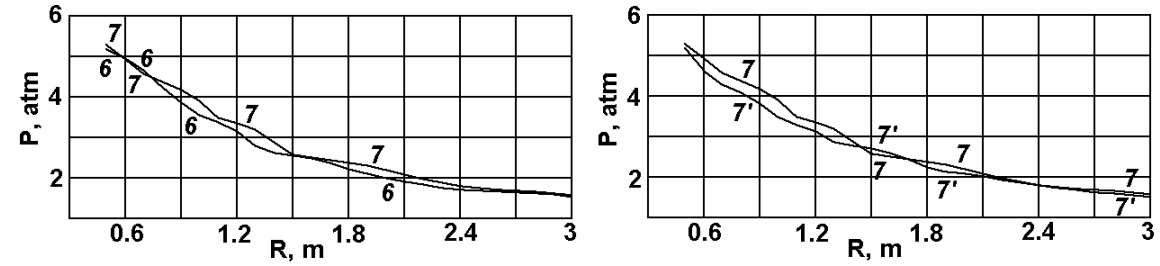

Figure 38. Comparison between the mitigation curves for an explosion of a charge surrounded by air-water sandwiches. Calculations with the Set-ups 6 and 7 keep the water mass constant. Two computational momentum-exchange options are compared for Set-up 7. These are identified as 7 and 7′

The present CTH calculations have been conducted for a multi-material environment in the computational domain that allowed the code to treat pressure and temperature separately for each material (option MMP in the CTH code [21]). Another option, which is declared by [21] as a more suitable approach for materials with contrast compressibilities, allows the pressure relaxation to be achieved during a time step (option MMP2 in the CTH code). All the set-ups have also been calculated using this option and the most divergent case, which is presented by curve 7′ that corresponds to the calculation with the option MMP2 for Set-up 7 in Table 2, is shown in Fig. 38 (comparison between the attenuation curves 7 and 7′). Thus, a choice of this numerical option within a general single-phase approach does not affect the general conclusions from this analysis area. Calculations for several selected problem set-ups, using a refined numerical mesh, have shown that the number of cells used in the present calculations provides numerical convergence; slight deviations between the mitigation curves during this analysis have been observed only at ranges not exceeding R≈0.6 m.

A more detailed analysis of the influence of the mass redistribution was conducted by introducing a mitigant as a double air-water sandwich (Set-ups 8 and 9); the corresponding mitigation curves are shown in Fig. 39. It is seen that the distribution of water into two different sub-layers separated by air gaps, while keeping the same water-to-charge mass ratio as in the Set-up 6, results in different attenuation relationships, particularly in the close-in range. Even at a large stand-off distance, a slightly different attenuation relationship has been observed for Set-ups 8 and 9 (results of the Set-up 8 converge to the results of the Set-up 6). An increase of water thickness from Set-ups 8 to 9 slightly increases the blast mitigation performance; however, the water thickness still does not reach the value of 1.25 produced by the single air-water sandwich, and has a worse

performance than even the doubled air-water sandwich with the water thickness value of 0.49 (Set-up 8). Thus, using even this simple single-phase multi-material consideration, a conclusion can be made about the importance of water breakdown and evaporation, which were not considered in the majority of the available analyses that have been reported to date.

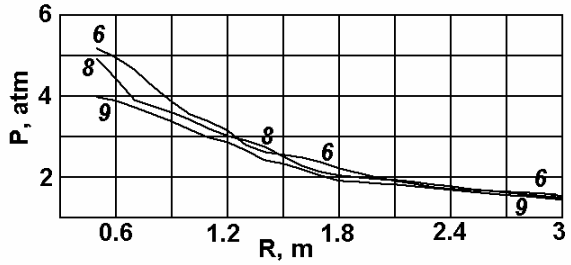

Figure 39. Comparison between the mitigation curves for an explosion of a charge surrounded by an air-water and a double air-water sandwich. Calculations with the Set-ups 6, 8 and 9 keep water mass constant

In summary, an increase in mitigation water mass generally enhances mitigation performance. However, comparison of the mitigation curves for different distribution arrangements for the mitigant, suggests that phase transformation and water breakdown mechanisms are the key factors affecting overall mitigation performance.

7. Conclusions

It has been shown that confinement around a mitigation experiment significantly affects the resulting explosive blast pressure outcomes. However, the attenuation curves in the close-in range can be confidently assessed with the present data results, and the comparative analysis in the close-in range can be extended to free-field conditions.

Misalignment between the pressure gauge mounting baffle and the blast wave flow results in a dynamic pressure contribution that increases with blast wave inflow pressure and non-steady inflow amplifies this factor. Keeping in mind the fixed gauge arrangement for the present series of tests, possible gauge set-up misalignment should introduce a consistent error with a corresponding contribution to the comparative analysis. However, the error induced by non-equilibrium flow is likely to be more severe for bulk mitigating liquids (for example, further divergence from equilibrium with the water mass increase can be seen from the mitigation curves obtained numerically in the previous section). Therefore, a larger misalignment error should be expected for the bulk mitigating cases in the close-in range.

Numerical analysis has shown that phase transformation and water breakdown could be the key factors that have to be considered for in the development of improved blast mitigation systems/techniques (unfortunately, multi-material model approaches in typical hydrocodes cannot currently simulate the fluid droplet breakdown mechanisms and

attenuation of blast transmitted through two-phase media, such as the gas-liquid systems). This conclusion is confirmed by the present numerical study, which showed that the liquid mass is not the only factor affecting blast wave mitigation. Tests with bulk water and glycerine, where improved mitigation performance was observed for a reduced mass of glycerine, also indicates the criticality of the phase transformation and liquid breakdown mechanisms for mitigation performance enhancement.

From the present study it is clear that improved blast mitigation could be achieved in a close-in range to the IED. The mitigation process is managed by a variety of physical mechanisms determined by the design features of a mitigation device, the mitigant's physical properties, and the IED's environment. The interaction and interdependence of these factors consequently results in a number of uncertainties caused by the individual and combined influences of these mechanisms, and the relative importance of the mechanisms should be assessed individually for a specific mitigation device in relation to the class of IED.

Thus, the study results show that a further research of an influence of the two-phase mechanisms on the peak overpressure attenuation that characterises blast mitigation is required. This includes the blast attenuation/amplification contributions from specific mitigants and charge confinement. Another important issue associated with protection to personnel and structures at a large stand-off distance is a long-range momentum transfer of the mitigant's phase to the targets. This issue needs to be considered in future more thoroughly as well.

8. Acknowledgements

The authors acknowledge help in conducting tests by D. Harris, J. Freundt, and I. Rogers.

9. References

1. Allen R.M., Kirkpatrick D.J., Longbottom A.W., Milne A.M., and Bourne N.K., Experimental and Numerical Study of Free-Field Blast Mitigation, in Shock Compression of Condensed Matter 2003, M.D. Furnish, Y.M. Gupta, and J.W. Forbes, Eds., 2004, American Institute of Physics: Melville, New York. p. 823-826.
2. Aizik F., Ben-Dor G., Elperin T., Igra O., and Mond M., Attenuation Law of Planar Shock Waves Propagating Through Dust-Gas Suspensions, AIAA J., v. 33, n. 5, 1995, pp. 953-955.
3. Aizik F., Ben-Dor G., Elperin T., and Igra O., General Attenuation Laws for Spherical Shock Waves in Pure and Dusty Gases, AIAA J., v. 39, n. 5, 2001, pp. 969-971.
4. Shin Y.S., Lee M., Lam K.Y., and Yeo K.S., Modeling mitigation effects of watershield on shock waves, Shock and Vibration, v. 5, n. 4, 1998, pp. 225-234.

5. Chong W.K., Lam K.Y., Yeo K.S., Liu G.R., and Chong O.Y., A comparison of simulation's results with experiment on water mitigation of an explosion, Shock and Vibration, v. 6, n. 2, 1999, pp. 73-80.
6. Liu M.B., Liu G.R., and Lam K.Y., Investigations into water mitigation using a meshless particle method, Shock Waves, v. 12, n. 3, 2002, pp. 181-195.
7. Zhao H.Z., Lam K.Y., and Chong O.Y., Water mitigation effects on the detonations in confined chamber and tunnel system, Shock and Vibration, v. 8, n. 6, 2001, pp. 349-355.
8. Cheng M., Hung K.C., and Chong O.Y., Numerical study of water mitigation effects on blast wave, Shock Waves, v. 14, n. 3, 2005, pp. 217-223.
9. Ball G.J. and East R.A., Shock and blast attenuation by aqueous foam barriers: influences of barrier geometry, Shock Waves, v. 9, n. 1, 1999, pp. 37-47.
10. Schwer D.A. and Kailasanath K., Water-Mist Mitigation of Quasi-Static Pressure Buildup in Enclosures Subjected to an Explosion, In: Proc. 20th Int. Colloquium on the Dynamics of Explosions & Reactive Systems (ICDERS), July 31 – August 5, 2005, McGill University, Montreal, Canada.
11. Kailasanath K. and Schwer D., Shock Attenuation Using Water Mists, In: Proc. 19th Int. Colloquium on the Dynamics of Explosions & Reactive Systems (ICDERS), Paper 64, July 27 – August 1, 2003, Hakone, Kanagawa, Japan.
12. Malvar L.J. and Tancreto J.E., Analytical and test results for water mitigation of explosion effects, In: Proc. the 28th DoD Explosives Safety Seminar, 1998, Orlando, FL, USA.
13. Joachim C.E. and Lunderman C.V., Blast Suppression with Water: Results of Small-Scale Test Program, In: CD-ROM Proc. 15th Int. Symp. On Military Aspects of Blast and Shock (MABS 15), ed. by D. Bergeron, Paper SB03, 1997, Banff, Alberta, Canada.
14. Rinaudo M.A. Smith P.D., and Rose T.A., The Attenuation of Blast Resultants Using Water, In: CD-ROM Proc. 15th Int. Symp. On Military Aspects of Blast and Shock (MABS 15), ed. by D. Bergeron, Paper SB04, 1997, Banff, Alberta, Canada.
15. Frolov S.M. and Gel'fand B.E., Problem of Detonation Suppression by Mans of Bankets and Foams, Combustion, Explosion, and Shock Waves (Fizika Gorenia I Vzryva), v. 27, n. 6, 1991, pp. 756-763.
16. Gel'fand B.E., Sil'nikov M.V., Mikhailin A.I., and Orlov A.V., Attenuation of Blast Overpressures from Liquid in an Elastic Shell, Combustion, Explosion, and Shock Waves (Fizika Gorenia I Vzryva), v. 37, n. 5, 2001, pp. 607-612.
17. Gelfand B.E. and Silnikov M.V., The selection of the effective blast reduction method when detonating explosives, J. de Phys. IV France, 2002, v. 12, n. 7, pp. Pr7-371 – Pr7-374.
18. Gelfand B.E., Silnikov M.V., Mikhailin A.I., and Orlov A.V., Blast inhibitors with transformation of blast waves by two-phase medium, In: CD-ROM Proc. 18th Int. Symp. On Military Aspects of Blast and Shock (MABS 18), Septebmber 27-October 1, 2004, Bad Reichenhall, Germany.
19. Smith S., Manasseh R., and Wu J., PDPA Measurement of Droplet Size Distributions from Spray Nozzles, Report to DSTO, 2005, CMIT2005-391, CSIRO, Melbourne.
20. IFSAS-II User Manual, Martec Ltd., Halifax, NS, Canada, 2002.

21. Bell R.L., Baer M.R., Brannon R.M., Crawford D.A., Elrick M.G., Hertel, Jr. E.S., Schmitt R.G., Silling S.A., and Taylor P.A., CTH User's Manual and Input Instructions, Version 7.1 (Internal Report), CTH Development Project, Sandia National Laboratories, Albuquerque, NM, USA, 2006.

DISTRIBUTION LIST

"As per the Research Library's *Policy on electronic distribution of official series reports* (http://web-vic.dsto.defence.gov.au/workareas/library/aboutrl/roles&policies/mission.htm) Unclassified (both Public Release and Limited), xxx-in-confidence and Restricted reports and their document data sheets will be sent by email through DRN to all recipients with Australian defence email accounts who are on the distribution list apart from the author(s) and the task sponsor(s). Other addressees and Libraries and Archives will also receive hardcopies."

Experimental Study of Blast Mitigation in a Water Mist

A.D. Resnyansky and T.G. Delaney

AUSTRALIA

DEFENCE ORGANISATION	**No. of copies**
Task Sponsor Benjamin Kwok NSST Unit, Dept of the Prime Minister and Cabinet 3 – 5 National Circuit, BARTON ACT 2600	1 Printed
S&T Program	
Chief Defence Scientist	1
Deputy Chief Defence Scientist Policy	1
AS Science Corporate Management	1
Director General Science Policy Development	1
Counsellor Defence Science, London	Doc Data Sheet
Counsellor Defence Science, Washington	Doc Data Sheet
Counsellor Defence Science, Thailand	Doc Data Sheet
Scientific Adviser Joint	1
Navy Scientific Adviser	1
Scientific Adviser – Army	1
Air Force Scientific Adviser	Doc Data Sheet
Scientific Adviser to the DMO	1
Chief of Weapons Systems Division	Doc Data Sht & Dist List
Research Leader - N. Burman WSD, 307 EOP, DSTO-Edinburgh	Doc Data Sht & Dist List
Head of WE Group WSD, 307 EOP, DSTO-Edinburgh	1
Task Manager - J. Waschl WSD, 307 EOP, DSTO-Edinburgh	1
Author: A. Resnyansky WSD, 307 EOP, DSTO-Edinburgh	1 Printed

Author: T. Delaney WSD, 307 EOP, DSTO-Edinburgh	1 Printed
S. Weckert WSD, 307 EOP, DSTO-Edinburgh	1 Printed

DSTO Library and Archives

Library Fishermans Bend	Doc Data Sheet
Library Edinburgh	2 printed
Defence Archives	1 printed
Library, Sydney	Doc Data Sheet
Library, Stirling	Doc Data Sheet
Library Canberra	Doc Data Sheet

Capability Development Group

Director General Maritime Development	Doc Data Sheet
Director General Capability and Plans	Doc Data Sheet
Assistant Secretary Investment Analysis	Doc Data Sheet
Director Capability Plans and Programming	Doc Data Sheet

Chief Information Officer Group

Head Information Capability Management Division	Doc Data Sheet
Director General Australian Defence Simulation Office	Doc Data Sheet
AS Information Strategy and Futures	Doc Data Sheet
Director General Information Services	Doc Data Sheet

Strategy Executive

Assistant Secretary Strategic Planning	Doc Data Sheet
Assistant Secretary International and Domestic Security Policy	Doc Data Sheet

Navy

Maritime Operational Analysis Centre, Building 89/90 Garden Island Sydney NSW Deputy Director (Operations) Deputy Director (Analysis)	Doc Data Sht & Dist List
Director General Navy Capability, Performance and Plans, Navy Headquarters	Doc Data Sheet
Director General Navy Strategic Policy and Futures, Navy Headquarters	Doc Data Sheet

Air Force

SO (Science) - Headquarters Air Combat Group, RAAF Base, Williamtown NSW 2314	Doc Data Sht & Exec Summary
Staff Officer Science Surveillance and Response Group	Doc Data Sht & Exec Summary

Army

Australian National Coordination Officer ABCA (AS NCO ABCA), Land Warfare Development Centre, Puckapunyal	Doc Data Sheet
J86 (TCS GROUP), DJFHQ	Doc Data Sheet
SO (Science) - Land Headquarters (LHQ), Victoria Barracks NSW	Doc Data Sht & Exec Summary
SO (Science) – Special Operations Command (SOCOMD), R5-SB-15, Russell Offices, Canberra	Doc Data Sht & Exec Summary & Dist List
SO (Science), Deployable Joint Force Headquarters (DJFHQ) (L), Enoggera QLD	Doc Data Sheet

Joint Operations Command

Director General Joint Operations	Doc Data Sheet
Chief of Staff Headquarters Joint Operations Command	Doc Data Sheet
Commandant ADF Warfare Centre	Doc Data Sheet
Director General Strategic Logistics	Doc Data Sheet

Intelligence and Security Group

Assistant Secretary Concepts, Capability and Resources	1
DGSTA, Defence Intelligence Organisation	1
Manager, Information Centre, Defence Intelligence Organisation	1
Director Advanced Capabilities, DIGO	Doc Data Sheet

Defence Materiel Organisation

Deputy CEO	Doc Data Sheet
Head Aerospace Systems Division	Doc Data Sheet
Head Maritime Systems Division	Doc Data Sheet
Program Manager Air Warfare Destroyer	Doc Data Sheet
Guided Weapon & Explosive Ordnance Branch (GWEO)	Doc Data Sheet
CDR Joint Logistics Command	Doc Data Sheet

OTHER ORGANISATIONS

National Library of Australia	1
NASA (Canberra)	1

UNIVERSITIES AND COLLEGES

Australian Defence Force Academy	
Library	1
Head of Aerospace and Mechanical Engineering	1
Hargrave Library, Monash University	Doc Data Sheet

OUTSIDE AUSTRALIA

INTERNATIONAL DEFENCE INFORMATION CENTRES

US Defense Technical Information Center	1
UK Dstl Knowledge Services	1
Canada Defence Research Directorate R&D Knowledge & Information Management (DRDKIM)	1
NZ Defence Information Centre	1
Dr. Eugene S. Hertel Jr. Thermal and Reactive Processes Dpt, Sandia National Laboratories, PO Box 5800, Albuquerque, NM 87185-0836, USA	1 Printed
Prof. E. I. Romensky Department of Aerospace Sciences School of Engineering, Cranfield University Bedfordshire MK43 0AL, UNITED KINGDOM	1 Printed
Mr. David V. Ritzel 19 Laird Ave North, Amherstburg, Ontario N9V 2T5, Canada	1 Printed

ABSTRACTING AND INFORMATION ORGANISATIONS

Library, Chemical Abstracts Reference Service	1
Engineering Societies Library, US	1
Materials Information, Cambridge Scientific Abstracts, US	1
Documents Librarian, The Center for Research Libraries, US	1

SPARES	5 Printed

Total number of copies: 40 Printed: 15 PDF: 25

DEFENCE SCIENCE AND TECHNOLOGY ORGANISATION
DOCUMENT CONTROL DATA

1. PRIVACY MARKING/CAVEAT (OF DOCUMENT)

2. TITLE

Experimental Study of Blast Mitigation in a Water Mist

3. SECURITY CLASSIFICATION (FOR UNCLASSIFIED REPORTS THAT ARE LIMITED RELEASE USE (L) NEXT TO DOCUMENT CLASSIFICATION)

Document	(U)
Title	(U)
Abstract	(U)

4. AUTHOR(S)

A.D. Resnyansky and T.G. Delaney

5. CORPORATE AUTHOR

DSTO Defence Science and Technology Organisation
PO Box 1500
Edinburgh South Australia 5111 Australia

6a. DSTO NUMBER	6b. AR NUMBER	6c. TYPE OF REPORT	7. DOCUMENT DATE
DSTO-TR-1944	AR-013-799	Technical Report	November 2006

8. FILE NUMBER	9. TASK NUMBER	10. TASK SPONSOR	11. NO. OF PAGES	12. NO. OF REFERENCES
2006/1163279/1	COM 04/283	Benjamin Kwok PM&C	32	21

13. URL on the World Wide Web

http://www.dsto.defence.gov.au/corporate/reports/DSTO-TR-1944.pdf

14. RELEASE AUTHORITY

Chief, Weapons Systems Division

15. SECONDARY RELEASE STATEMENT OF THIS DOCUMENT

Approved for public release

OVERSEAS ENQUIRIES OUTSIDE STATED LIMITATIONS SHOULD BE REFERRED THROUGH DOCUMENT EXCHANGE, PO BOX 1500, EDINBURGH, SA 5111

16. DELIBERATE ANNOUNCEMENT

No Limitations

17. CITATION IN OTHER DOCUMENTS Yes

18. DSTO RESEARCH LIBRARY THESAURUS http://web-vic.dsto.defence.gov.au/workareas/library/resources/dsto_thesaurus.htm

Blast mitigation, water mist, improvised explosive devices, countermeasures

19. ABSTRACT

This report presents results of experiments on the mitigation of explosive blast using water mist. Water mists in the present study were produced by nozzles distributed around a test arena. Tests were conducted using different water mist sizes and nozzle arangements to evaluate blast mitigation effects for in-air bare explosive charges as well as charges submerged in water and glycerine. The effects on blast wave pressure results due to the experimental blast pressure gauge mounting and set-up, as well as due to the effects of confinement in the test area, are analysed and discussed. Blast attenuation was evaluated using the CTH hydrocode and concluded that the phase transformation and mitigant liquid breakdown mechanisms, under expansion by the blast products, must be considered in order to model blast mitigation adequately and to accurately evaluate mitigation effects at large stand-off distances.